THE SUZAKU OBSERVATION OF THE NUCLEUS OF THE RADIO-LOUD ACTIVE GALAXY CENTAURUS A: CONSTRAINTS ON ABUNDANCES OF THE ACCRETING MATERIAL

A. Markowitz[1,2], T. Takahashi[3], S. Watanabe[3], K. Nakazawa[3], Y. Fukazawa[4], M. Kokubun[5], K. Makishima[5,6], H. Awaki[7], A. Bamba[6], N. Isobe[6], J. Kataoka[8], G. Madejski[9,10], R. Mushotzky[1], T. Okajima[1], A. Ptak[11] J.N. Reeves[1,11], Y. Ueda[12], T. Yamasaki[4], T. Yaqoob[11]

[1] X-ray Astrophysics Laboratory, Code 662, NASA/Goddard Space Flight Center, Greenbelt, MD 20771, USA; agm@milkyway.gsfc.nasa.gov
[2] NASA Post-doc Research Associate
[3] Institute of Space and Astronautical Science, JAXA, Sagamihara, Kanagawa 229-8510, Japan
[4] Department of Physics, Hiroshima University, 1-3-1 Kagamiyama, Higashi-Hiroshima, 739-8526, Japan
[5] Department of Physics, Graduate School of Science, University of Tokyo, Hongo 7-3-1, Bunkyo, 113-0033, Japan
[6] The Institute of Physical and Chemical Research (RIKEN), 2-1 Hirosawa, Wako, 351-0198, Japan
[7] Department of Physics, Faculty of Science, Ehime University, Bunkyo-cho, Matsuyama, Ehime 790-8577, Japan
[8] Department of Physics, Tokyo Institute of Technology, Meguro, Tokyo 152-8551, Japan
[9] Stanford Linear Accelerator Center (SLAC), 2575 Sand Hill Road, Menlo Park, CA 94025, USA
[10] Kavli Institute for Particle Astrophysics and Cosmology, Stanford University, Stanford, CA 94305, USA
[11] Department of Physics and Astronomy, Johns Hopkins University, Baltimore, MD 21218, USA
[12] Department of Astronomy, Kyoto University, Sakyo-ku, Kyoto 606-8502, Japan

ABSTRACT

A *Suzaku* observation of the nucleus of the radio-loud AGN Centaurus A in 2005 has yielded a broadband spectrum spanning 0.3 to 250 keV. The net exposure times after screening were: 70 ks per X-ray Imaging Spectrometer (XIS) camera, 60.8 ks for the Hard X-ray Detector (HXD) PIN, and 17.1 ks for the HXD-GSO. The hard X-rays are fit by two power-laws of the same slope, absorbed by columns of 1.5 and 7×10^{23} cm^{-2} respectively. The spectrum is consistent with previous suggestions that the power-law components are X-ray emission from the sub-pc VLBI jet and from Bondi accretion at the core, but it is also consistent with a partial covering interpretation. The soft band is dominated by thermal emission from the diffuse plasma and is fit well by a two-temperature VAPEC model, plus a third power-law component to account for scattered nuclear emission, jet emission, and emission from X-ray Binaries and other point sources. Narrow fluorescent emission lines from Fe, Si, S, Ar, Ca and Ni are detected. The Fe Kα line width yields a 200 light-day lower limit on the distance from the black hole to the line-emitting gas. Fe, Ca, and S K-shell absorption edges are detected. Elemental abundances are constrained via absorption edge depths and strengths of the fluorescent and diffuse plasma emission lines. The high metallicity ([Fe/H]=+0.1) of the circumnuclear material suggests that it could not have originated in the relatively metal-poor outer halo unless enrichment by local star formation has occurred. Relative abundances are consistent with enrichment from Type II and Ia supernovae.

Subject headings: galaxies: active — X-rays: galaxies — galaxies: individual (NGC 5128)

1. INTRODUCTION

The radio-loud active galactic nucleus (AGN) Centaurus A (NGC 5128) is one of the most extensively-studied AGNs at all wavebands, thanks to its proximity (distance of 3.8 ± 0.4 Mpc, Rejkube 2004; $1' = 1$ kpc) and brightness (2–10 keV flux typically $\sim 2 \times 10^{-10}$ erg cm^{-2} s^{-1}). Cen A features the nearest AGN jet and is considered a prototypical FR I radio galaxy. Its radio structure consists of extended kpc-scale outer, middle, and inner radio

lobes, fed by a one-sided kpc-scale jet. The jet is at an angle of $\sim 60°$ to the line of sight, leading to its description as a 'misaligned' BL Lac object (e.g., Bailey et al. 1986). VLBI observations have also revealed a sub-pc jet and unresolved (~ 0.1pc) core (Tingay et al. 1998; see also Israel 1998 for a review).

The host galaxy of Cen A is a giant elliptical with a pronounced optical dust lane that obscures the inner few kpc and is believed to be an edge-on disk structure (Quillen et

1

al. 1992). The inner dust disk, with associated young stars, H II regions, and other ionized gas, is the site of vigorous star formation, e.g., observed along the edges of the inner disk (e.g., Ebneter & Balick 1983, Dufour et al. 1979). The dust disk is interpreted as the result of a merger between a large elliptical and a gas-rich disk galaxy at least a Gyr ago (e.g., Israel 1998). Infrared studies are necessary to reveal the compact, pc-scale core (e.g., Karovska et al. 2003). NIR studies (e.g, Schreier et al. 1998) have revealed a circumnuclear disk tens–hundreds of pc wide, surrounding the central black hole. Stellar kinematic studies indicate a black hole mass near 2×10^8 $M_\odot$ (Silge et al. 2005)

Previous studies of the nuclear X-ray emission from $\sim$4 keV to several hundred keV (e.g., Rothschild et al. 1999) have established the presence of a non-thermal, power-law continuum whose origin is not certain. It could be a signature of accretion, or it could be associated with jet emission processes, e.g., synchrotron or inverse Compton emission from the sub-pc VLBI jet.

Below $\sim$4 keV, the X-ray continuum emission undergoes moderately heavily absorption, though the nature of the X-ray obscuring material is not certain, i.e., it could have a sky-covering fraction of 1 as seen from the central X-ray source or it could be in a form of a dusty torus. Rothschild et al. (2006) have noted $\sim$50% variations in the absorbing column over $\sim$20 years, and suggested that the nucleus is seen through the edges of a warped, rotating disk. The strong X-ray absorption makes Cen A relatively unique: the vast majority of FR I radio galaxies possess relatively weak X-ray absorbing columns ($\lesssim 10^{20-21}$ cm^{-2}). Heavy X-ray absorption, meanwhile, is usually seen only in FR II radio galaxies, though it is not yet clear if the dichotomy in X-ray absorption properties has the same origin as the FR I/II dichotomy, e.g., differing accretion modes (Donato et al. 2004, Balmaverde et al. 2006, Evans et al. 2006).

Previous X-ray spectral fits to the nucleus of Cen A center on one or more power-laws, with varying degrees of absorption. For instance, using *ROSAT* and *ASCA*, Turner et al. (1997) suggested that one plausible description of the nuclear emission is a partial-covering model, wherein the nucleus is seen through three layers of absorption: 40%, 59%, and 1% of the nuclear emission is obscured by columns of 4, 1 and 0.01 $\times$ 10^{23} cm^{-2}, respectively. Using *Chandra*-HETGS and *XMM-Newton* observations, Evans et al. (2004) suggested a different interpretation. They fit the hard X-ray continuum spectrum by a heavily-absorbed power-law, thought to be associated with Bondi accretion at the core, plus a relatively less-absorbed power-law thought to be associated with the sub-pc VLBI jet, though they did not rule out the partial covering interpretation.

There is a prominent Fe Kα emission line at 6.4 keV, first noted by Mushotzky et al. (1978). It is narrow (e.g., FWHM = 2200$\pm$900 km s^{-1}, Evans et al. 2004), and its flux is historically nearly constant despite long-term continuum variations spanning a factor of $\sim$5 over 20 years (Rothschild et al. 1999), implying an origin for the line which is distant from the origin of the variable continuum.

The soft X-ray emission within $\sim$ 6 kpc of the nucleus of Cen A consists of both diffuse and point-like emission. There is diffuse emission is associated with the kpc-scale

jet extending from $<$ 60 pc to the NE radio lobe (e.g., Kraft et al. 2002), as well as from thermal gas which surrounds the nucleus out to a radius of roughly 6 kpc. Point-like emission is associated with several dozen knots in the kpc-scale jet (e.g., Kataoka et al. 2006) as well as from a population of X-ray Binaries (e.g., Kraft et al. 2000). A soft X-ray spectrum covering the inner few kpc is thus expected to contain both power-law continuum emission from the jet and point-like sources and line-like emission associated with the thermal gas. For instance, Turner et al. (1997) modeled the soft X-rays with a 0.6 keV thermal plasma component, a 5 keV component associated with emission from a population of X-ray Binaries, and a power-law jet component.

In this paper, we report on an observation of Cen A made with the *Suzaku* observatory in August 2005. The combination of the X-ray Imaging Spectrometer (XIS) CCD and the Hard X-ray Detector (HXD) instruments have yielded a broadband spectrum covering 0.3 to 250 keV, allowing us to deconvolve the various broadband emitting and absorbing components in this object. Furthermore, the exceptional response of the XIS CCD and high signal-to-noise ratio of this observation allow us to study narrow emission lines in great detail. This observation has also yielded the highest quality soft X-ray spectrum of Cen A obtained so far. §2 gives a brief overview of the *Suzaku* observatory, and describes the observation and data reduction. §3 describes the spectral fits. The results are discussed in §4, and a brief summary is given in §5.

2. OBSERVATIONS AND DATA REDUCTION

The nucleus of Cen A was observed by *Suzaku* from 2005 August 19 at 03:30 UT until August 20 at 09:50 UT, and in fact was the first light target for the HXD. *Suzaku* was launched 2005 July 10 into a low-Earth orbit. It has four X-ray telescopes (XRTs; Serlemitsos et al. 2007), each with a spatial resolution of 2$'$ (HPD). The XRTs focus X-rays onto four X-ray Imaging Spectrometer (XIS; Koyama et al. 2007) CCDs, which are sensitive to 0.2–12 keV X-rays on a 18$'$ by 18$'$ field of view, contain 1024 by 1024 pixel rows each, and feature an energy resolution of $\sim$140 eV at 6 keV. Three CCDs (XIS0, 2 and 3) are front-illuminated (FI), the fourth (XIS1) is back-illuminated (BI) and features an enhanced soft X-ray response. The XRT/XIS combination yields effective areas per detector of roughly 330 cm^2 (FI) or 370 cm^2 (BI) at 1.5 keV, and 160 cm^2 (FI) or 110 cm^2 (BI) at 8 keV. Each XIS is equipped with two ^{55}Fe calibration sources which produce fluorescent Mn Kα and Kβ lines and are located at the CCD corners. *Suzaku* also features a non-imaging, collimated Hard X-ray Detector (HXD; Takahashi et al. 2007); its two detectors, PIN and GSO, combine to yield sensitivity from $\sim$10 to $\sim$700 keV. Further details of the *Suzaku* observatory are given in Mitsuda et al. (2007).

2.1. *XIS reduction*

The XIS data used in this paper were version 0.7 of the screened data (Fujimoto et al. 2007) provided by the Suzaku team. The screening is based on the following criteria: grade 0, 2, 3, 4, and 6 events were used, the CLEANSIS script was used to remove hot or flickering pixels, data collected within 256 s of passage through the

South Atlantic Anomaly (SAA) were discarded, and data were selected to be 5° in elevation above the Earth rim (20° above the day-Earth rim). The XIS-FI CCDs were in 2x2, 3x3 and 5x5 editmodes, for a net exposure time after screening of 71.5 (XIS0), 70.3 (XIS2) and 68.6 (XIS3) ks. XIS1 was in 3x3 and 5x5 modes, for a net exposure of 68.6 ks.

The source was observed at the nominal center position of the XIS. The XIS was kept in Normal Mode, but to reduce the risk of photon-pileup, the 1/4 Window Option was used: each CCD recorded 256 by 1024 pixel rows, with a readout time of 2 s, as opposed to 8 s when the full 1024 by 1024 window is used. For each XIS, we extracted a 2′ radius centered on the source. Spectra were binned to a minimum of 50 counts bin^{-1} to allow use of the χ^2 statistic.

The count rates observed over the full XIS band were 5.0 ct s^{-1} (average of XIS0, 2 and 3) or 4.3 ct s^{-1} (XIS-BI). These count rates are far below the limit for photon-pileup in 1/4 Window Mode, $\sim$ 12.5 ct s^{-1}. Furthermore, extracting over annular regions with inner and outer radii of 0.4′ and 2′, respectively, yielded spectra identical in shape to those extracted over 2′ circular regions, indicating that pile-up was negligible.

Because the soft diffuse emission in Cen A covers nearly the entire read-out area of the CCD, we used observations of the North Ecliptic Pole (NEP) to extract a background spectrum. *Suzaku* observed the NEP on 2005 September 2 to 4. There was a brief, sharp flare during the NEP observation, consistent with evidence for solar wind charge exchange emission (see Fujimoto et al. 2007). Removing that flare and applying the same screening criteria as above yielded a net exposure time of 93.9 (XIS0), 108.5 (XIS1), 93.3 (XIS2), 96.6 (XIS3) ks. We extracted data over a 2′ circle. The NEP is known to contain soft X-ray emission lines (see e.g., Fujimoto et al. 2007), but they are much fainter than those of Cen A (see §3). The O VII and O VIII lines in Cen A are a factor of roughly 10 (20) higher compared to NEP as seen in the XIS-BI (XIS-FIs). Lines near 0.8–0.9 keV such as Fe L XVII and Ne IX in Cen A are typically $\sim$60 (100) times brighter in Cen A compared to the NEP as seen in the XIS-BI (XIS-FIs).

Average 0.5–2.0 keV count rates for the NEP observation were 0.004, 0.009, 0.004 and 0.003 count s^{-1} for XIS0, 1, 2 and 3, respectively; average 2–10 keV count rates were 0.005, 0.012, 0.005 and 0.004 count s^{-1}, respectively.

Response matrices and ancillary response files (ARFs) were generated for each XIS independently using XISSIMRMFGEN and XISSIMARFGEN version 2006-10-26 (Ishisaki et al. 2007). The ARF generator takes into account the level of hydrocarbon contamination on the optical blocking filter. However, the Cen A observation occurred very early in the *Suzaku* mission, and the level of contamination was quite low: we estimate a carbon column density of only $\sim$0.1, 0.2, 0.3 and 0.5$\times10^{18}$ cm^{-2} for XIS0, 1, 2 and 3, respectively.

A consequence of observing with the 1/4 Window Option is that there are no ^{55}Fe calibration source lines on the CCD. This leads to a higher systematic uncertainty in the energy scale compared to normal mode (where it is a few tenths of a percent at most). To estimate the instrument resolution, we used the calibration source lines from a 77 ks observation of MCG–6-30-15, observed in Normal Mode with no window option immediately prior to Cen A. We fit the calibration source spectra with three Gaussians. Two Gaussians were for the Mn Kα doublet (expected energies 5.899 keV and 5.888 keV), with energy centroids fixed to be 11 eV apart, and the higher energy line flux set to twice that of the lower energy one. The third Gaussian was used to model the Kβ line, expected at 6.490 keV. We found the average of all the calibration line widths σ to be 9^{+6}_{-2} eV; residual width may be due e.g., to imperfect CTI correction.

The positional accuracy of *Suzaku* is $\sim$1′ at present, as the spacecraft has been known to exhibit small attitude variations ("wobble"). We checked to make sure that the effect of these attitude variations was not significant, given that the 1/4 Window Option was used throughout the observation. We generated light curves by extracting over radii of 1.5′ and 1.0′ and looked for variations on the orbital timescale, but found nothing significant.

Average 0.5–2.0 keV net source count rates were 0.24, 0.35, 0.25, and 0.25 count s^{-1} for XIS0, 1, 2, and 3, respectively. Average 2–10 net source count rates were 4.7, 4.4, 4.5, and 4.5 count s^{-1} for XIS0, 1, 2, and 3, respectively. Figure 1 shows 2–10 keV light curves for each XIS. During the observation, the 2–10 keV source flux increased by only 10%, with fractional variability amplitudes $F_{\rm var}$ (see Vaughan et al. 2003 for definition) of 3.7 ± 0.2 %, 3.4 ± 0.2 %, 3.1 ± 0.2 %, and 3.3 ± 0.2 % for XIS0, 1, 2, and 3, respectively. The 0.5–2.0 keV flux (determined from model fits; see §3) was 2.33×10^{-12} erg cm^{-2} s^{-1}. The 2–10 keV flux was 2.12×10^{-10} erg cm^{-2} s^{-1}.

2.2. *HXD reduction*

The PIN and GSO source spectra were extracted from cleaned version 1.2 (pre-1.2-r1) HXD event files provided by the HXD instrument team. We first discuss the PIN extraction. Data were selected according to the following criteria: at least 500 s since SAA passage, COR $\geq$ 8 GV, and day- and night-Earth elevation angles each $\geq$5°. Instrumental (non-X-ray) background spectra for the PIN were provided by the HXD Team ("Background D" model) generated from a time-dependent model.[13] The model utilized the count rate of upper discriminators as the measure of cosmic ray flux that passed through the silicon PIN diode and yielded background spectra based on a database of non X-ray background observations with the PIN (Fukazawa et al. 2007). The systematic uncertainty of the PIN is expected to be $<$5%. However, we note that Cen A is one of the brightest AGNs in the PIN energy range, and the effect of background subtraction error on the net source spectrum is relatively small. Both the source and background spectra were generated with identical good time intervals, and the exposures were corrected for instrument dead time (a $\sim$5% effect). This yielded a good time exposure of 60.8 ks. Data $<$ 12 keV were discarded due to noise contamination near the lower threshold of the PIN diode. Data above 76 keV were also discarded: the gain above

---

[13] Other recently-published *Suzaku* results have made use of the "Background A" model. However, observations occurring before September 2, 2005 had a hit-pattern width set to a shorter value compared to observations occurring after this date. Because applying the "Background A" model would yield an underestimate of the true non-X-ray PIN background, we instead use the "Background D" model.

an internal Bi Kα calibration line at 76 keV is not well-defined, though there is GSO data covering these energies. Further details of the HXD in-orbit performance are given in Kokubun et al. (2007). To model the contribution to the total background from the Cosmic X-ray Background (CXB), the spectrum of the form $9.0\times10^{-9}(E/3keV)^{-0.29}$ exp($-E/40keV$) erg cm^{-2} s^{-1} sr^{-1} keV^{-1} (Gruber et al. 1999) was used; the contribution in the 12–76 keV band was 1.1×10^{-11} erg cm^{-2} s^{-1}.

The spectrum was binned to a minimum of 400 count bin^{-1}. We used the response file ae_hxd_pinxinom_20060814.rsp. The 12–76 keV net source flux and count rate were 7.3×10^{-10} erg cm^{-2} s^{-1} and 1.21 count s^{-1}. The total (X-ray plus particle) background 12–76 keV flux and count rate were 6.9×10^{-10} erg cm^{-2} s^{-1} and 0.59 count s^{-1}. The orbitally-binned light curve is shown in Figure 1. The light curve generally increases in flux by ∼10–20% over the observation, matching the general trend shown by the XIS light curve, though shorter-timescale differences between the XIS and PIN light curves might be attributed to uncertainty associated with the PIN background. Figure 2 shows the net source, background, and total (source + background) spectra. The source spectrum is always at least 30% of the total up to ∼50 keV.

The HXD-GSO data were reduced in a manner similar to the HXD-PIN data. A key contributor to the GSO particle background is activation lines, e.g., delayed emission from radioactive isotopes induced inside the detector due to interaction with SAA particles. To minimize such emission, data taken within 6000 s of SAA passage were discarded; the background is the most reliable and the least variable during non-SAA orbits. This yielded a good time exposure of 17.1 ks. The 'Background D' model files provided by the HXD Team were used (Fukazawa et al. 2007). The CXB is expected to contribute insignificantly to the total GSO background and was ignored. Source and background spectra were both binned with GRPPHA following recommendations from the HXD Team[14].

The source was detected out to 250 keV; the GSO is sensitive down to roughly 45 keV. The 45–250 keV net source flux and count rate were 7.2×10^{-10} erg cm^{-2} s^{-1} and 0.83 count s^{-1}. The 45–250 keV background flux and count rate were 1.0×10^{-8} erg cm^{-2} s^{-1} and 9.1 count s^{-1}. Figure 1 shows the GSO light curve. Figure 2 shows the net source, background, and total (source + background) spectra. The source spectrum is always at least 5% of the total below 200 keV. The response file ae_hxd_gsoxinom_20060321.rmf was used.

Below 100 keV, the GSO field of view is $34'\times34'$ FWHM, the same as the PIN. Above 100 keV, the field of view increases with photon energy to a maximum of $4.5°\times4.5°$ FWHM and there is the possibility of source confusion. The nearest possible contaminating source is the blazar MS 1312.1-4221 = GRO J1312–42, located ∼2° west of Cen A. According to Steinle et al. (1998), the flux of MS 1312.1-4221 in the *Compton Gamma-Ray Observatory* (*CGRO*)-OSSE band (50-4000 keV) is likely less than a

tenth of Cen A's flux. MS 1312.1-4221 is much fainter at other X-ray bands as well: the 1 keV intensity is usually only 1–10% of the historically-observed Cen A intensities (Kinzer et al. 1995). We henceforth assume that the contamination from MS 1312.1-4221 is negligible in the GSO band.

3. SPECTRAL ANALYSIS

Given the $2'$ HPD of the XRT, the spectrum will contain blended contributions from multiple sources. Previous studies (e.g., Evans et al. 2004) have shown the hard X-rays[15] to be dominated by two power-laws; both hard X-ray components are constrained to lie within a few tenths of an arcsecond (∼5 pc) of the position of the unresolved radio core by *Chandra*-ACIS (Kraft et al. 2000). Contributions to the soft X-rays include thermal emission from the diffuse plasma plus diffuse emission from the kpc-scale jet, with contributions from a few of the innermost knots in the kpc-scale jet and other point sources resolved by *Chandra*-ACIS (Kraft et al. 2000; Kataoka et al. 2006). Each knot, however, is extremely faint in the soft X-rays ($\lesssim 6 \times 10^{-13}$ erg cm^{-2} s^{-1}; Feigelson et al. 1981).

The four XIS spectra were fit separately. 0.4–11.5 keV FI data and 0.3–11.5 keV BI data were included. We found it reasonable to keep the photon indices tied for all four XISes. while allowing the relative normalizations for XIS0 and XIS1 to each vary relative to that for XIS2 and 3, which were tied together (XIS3/XIS2 was always consistent with, and therefore fixed at, 1.00). XIS0/XIS2 was typically 1.06; XIS1/XIS2 was typically 0.96 (in our best-fit model, XIS0/XIS2 = 1.065±0.004 and XIS1/XIS2 = 0.951±0.003). We ignored 1.80–1.87 keV in the XIS FI spectra and 1.75–1.87 keV in the XIS BI spectrum due to uncertainties in calibration associated with the instrumental Si K edge. This means we cannot directly study the intrinsic neutral Si K edge in the absorbing material or any highly-ionized Si K lines expected due to the thermal plasma emission. The PIN/XIS2 and GSO/XIS2 normalizations were left free, but were usually close to 1.09 and 0.9–1.0, respectively, though results were not strongly dependent on these factors (in our best-fit model, PIN/XIS2 = 1.055±0.022 and GSO/XIS2 = 0.98±0.06). Preliminary results on the relative GSO/PIN normalization using the Crab suggest GSO/PIN = 0.84 (Yamasaki et al., in prep). Fixing GSO/PIN at 0.84 in the Cen A fits usually resulted in χ^2 increasing by $\lesssim5$; the photon index did not change significantly. We left the GSO/PIN normalization free to attain the lowest χ^2 possible. All errors on one interesting parameter correspond to $\Delta\chi^2 = 2.71$ (with all relative normalizations except XIS3/XIS2 left free). Observed spectral features in Cen A are redshifted by z = 0.001825 (Graham 1978), the value corresponding to Cen A's recessional velocity. To calculate luminosities, a redshift of 0.0009, corresponding to a luminosity distance of 3.8 Mpc (assuming H_0 = 70 km s^{-1} Mpc^{-1}) was used. Galactic absorption of 8.6×10^{20} cm^{-2} was included. The abundances of Lodders (2003) were used. Absolute abundances relative to solar values are denoted by $Z_{\rm Fe}$; a value

---

[14] group 0 24 25 25 26 2 27 28 2 29 31 3 32 35 4 36 38 3; group 39 42 4 43 46 4 47 51 5 52 56 5 57 62 6; group 63 68 6 69 75 7 76 83 8 84 91 8 92 100 9; group 101 110 10 111 121 11 122 134 13 135 147 13 148 162 15; group 163 178 16 179 196 18 197 216 20 217 238 22 239 262 24; group 263 288 26 289 317 29 318 349 32 350 384 35 385 422 38; group 423 465 43 466 511 46

[15] We henceforth denote "hard X-ray" emission as any intrinsic emission component above 2–3 keV, as opposed to describing emission detected solely with the HXD.

of 1 denotes solar abundance.

As shown below, the best model fit includes five overlapping broadband components, and changes in how one is fit can potentially cause changes in other components. Our strategy in finding the best-fit broadband model was to fit the hard band first, then extend it to the soft band. Relatively more narrow features (lines and edges) were explored later.

3.1. *Broadband fit*

We first fit the >3 keV emission with an absorbed power-law (henceforth denoted PL1) using ZVPHABS(CUTOFFPL) (Model 1). The power-law cutoff was kept fixed at 400 keV; abundances in the absorber were initially kept fixed at solar. Residuals are plotted in Figure 3. The slight hard excesses above $\sim$9 keV in the XIS spectra are associated with calibration uncertainties known at the time of this writing. Residuals in the GSO spectrum near 150–200 keV are likely associated with uncertainties in estimating the strengths of activation lines in the GSO background (lines at 153 and 196 keV are due to ^{153}Gd and ^{151m}Eu, respectively); see Kokubun et al. (2007) for further details. GSO residuals near 65 keV are likely associated with calibration uncertainties present at the time of this writing. Large residuals near the expected Fe Kα line were apparent. We then added Fe Kα and Kβ lines; the Kβ energy was fixed at 7.056 keV, its intensity was fixed at 0.13 times that of Kα, and the widths of the two lines were tied. χ^2/dof dropped from 10700/7135 to 7607/7132, but the residuals in the XIS band suggested the fit could be improved if we added a second, fainter absorbed power-law (PL2; Model 2). The photon index of the second power-law, Γ_2, was kept tied to that of PL1, Γ_1, for simplicity, but the absorbing column densities $N_{\rm H1}$ and $N_{\rm H2}$ were not. χ^2 dropped by over 140. PL1, with a 1 keV normalization $\sim$4 times that of PL2, was absorbed by a column $N_{\rm H1}$ near 1.0×10^{23} cm^{-2}; $N_{\rm H2}$ was near 5.0×10^{23} cm^{-2}. The photon index was $1.773^{+0.018}_{-0.015}$. Residuals to Model 2 are plotted in Figure 3.

We then included the soft band data, down to 0.3 keV. Several soft X-ray emission lines are prominent, and are especially well constrained with XIS1, as illustrated in Figure 4. Simply adding a third power-law (Model 3) to the soft X-rays thus did not yield an acceptable broadband fit. Table 1 shows results for the lines when each is fit with a Gaussian; we identify them as originating in O VII, O VIII, a blend of Fe XVII 3s–2p lines (the $^3P_1/^3P_2$ doublet and the $^1P_1$ line), a blend of Fe XVII 3d–2p lines ($^1P_1$ and $^3D_1$), Ne IX, Ne X and Mg XI. We can use the lines as a check of the absolute energy scale of the XIS. Assuming that in each He-like triplet, the resonant line is a factor of 2 in intensity greater than the forbidden line (roughly consistent with the plasma temperatures in our best-fit model, below), the measured energy centroids are within $\lesssim$16 eV of the expected energies. Additionally, the Fe Kα centroid is 6$\pm$3 eV from its expected energy.

The emission lines could be due to gas which is photo- or collisionally-ionized. A key to distinguishing between the resulting spectra is that collisional ionization usually leads to the presence of very strong Fe L emission, such as a narrow Fe XVII emission line near 0.83 keV and a Fe L emission "bump" near 0.7–0.9 keV. We modeled the

soft emission using XSTAR tables appropriate for emission from photo-ionized gas, assuming either one or two zones of photo-ionized gas. Fitting this model always left strong residuals due to improperly modeled Fe L emission, even when the Fe abundance was left as a free parameter (in which case values commonly pegged at an upper limit of 10). The best-fit models assuming either one or two zones had χ^2/dof values of 11600/9159 and 11000/9155, respectively.

Attempting to model the soft band emission with a single-temperature VAPEC component, with all abundances fixed at solar, also did not yield an acceptable fit. In Model 4, we tried two VAPEC components, henceforth denoted VAPEC1 and VAPEC2. The best-fit model had temperatures of $k_{\rm B}T \sim 0.2$ keV, to model the He- and H-like O lines, and $k_{\rm B}T \sim 0.6$ keV, to model the Fe L and He- and H-like Ne lines. However, χ^2/dof was still high, 10395/9160, and there were still large residuals <0.7 keV.

It is plausible that some optically-thin circumnuclear material may scatter some of the hard X-ray continuum; a scattered power-law component was included in the best-fit model of Turner et al. (2005), for instance. In addition to the two VAPEC components, we added a third power-law (PL3), with photon index Γ_3 tied to Γ_1, assuming that PL3 undergoes no absorption in excess of the Galactic column. χ^2/dof was high: 10158/9161. Untying Γ_3 improved the fit considerably: χ^2/dof fell to 9806.8/9158; Γ_3 was $1.16^{+0.13}_{-0.10}$ (Model 5).

However, it is plausible that PL3 does undergo some absorption in the host galaxy, so we added an ZVPHABS component to PL3, and refit with Γ_3 tied to Γ_1. χ^2/dof fell to 9798.9/9160. The column density of the third absorber, $N_{\rm H3}$, was $0.13\pm0.06 \times 10^{22}$ cm^{-2}. The 1 keV normalization of PL3 was 0.8% of the sum of the normalizations of PL1 and PL2. Untying Γ_3 improved the fit considerably: χ^2/dof fell to 9745.1/9159, Γ_3 was $1.28^{+0.08}_{-0.12}$, and $N_{\rm H3}$ was <0.03 $\times 10^{22}$ cm^{-2} (Model 6). All of the improvement in the fit when Γ_3 was thawed came at energies below 2 keV. PL3 likely represents a blend of scattered emission (likely $\lesssim$ 0.8% of the total nuclear hard X-ray continuum) plus X-ray emission associated with the kpc-scale jet, with perhaps some contribution from XRBs or ULXs in the inner 2 kpc of the host galaxy. As we have achieved a much better fit with collisional rather than photo-ionization models, we will henceforth assume the soft emission lines are collisional in nature, though we cannot rule out, e.g., that some portion of the O VII and O VIII emission lines may be due to photo-ionization, or that there may be a small contribution from O VII RRC to the observed Fe XVII 3s–2p emission complex at $0.732^{+0.004}_{-0.006}$ keV. For the moment, we adopt Model 6 as our new baseline broadband model. Best-fit parameters for Models 5 and 6 are listed in Table 2. Data/model residuals for Models 3, 4, and 6 are shown in Figure 5.

3.1.1. *Hard X-ray continuum emission*

Evans et al. (2004) fit the hard X-ray *Chandra* and *XMM-Newton* data with a dual power-law model, wherein Γ_1 and Γ_2 differed by about 0.3. We untied Γ_2 from Γ_1. However, compared to Model 6, χ^2 only dropped by 1.4, and the best-fit values of Γ_1 and Γ_2 were consistent; the uncertainty on Γ_2 was $\pm$0.24. In subsequent fits, we will

continue to fix $\Gamma_2=\Gamma_1$.

There has been no strong evidence from past observations for a strong Compton reflection hump in Cen A. We added a Compton reflection component to Model 6 using PEXRAV, keeping the input normalization equal to that of PL 1, the inclination fixed at 30°, the high-energy cutoff fixed at 400 keV, assuming solar abundances, and leaving the PIN/XIS2 normalization free. The best fit-model preferred a value of the reflection fraction R (defined as $\Omega/2\pi$, where Ω is the solid angle subtended by the reflector) of 0, with an upper limit of 0.05, consistent with previous suggestions that the Fe Kα line originates in Compton-thin material. This limit is identical to that obtained by Benlloch et al. (2001) using *Rossi X-ray Timing Explorer* (*RXTE*) data. Contour plots of R versus Γ_1 and versus the PIN/XIS2 relative instrument normalization are shown in Figure 6.

Using *CGRO*-OSSE, Kinzer et al. (1995) found evidence for a high-energy cutoff which appeared at 300 keV to $\sim$700 keV in the highest- to lowest-flux states, respectively. In addition, Steinle et al. (1998) fitted data combined from *CGRO* OSSE, COMPTEL and EGRET; one of the spectral breaks they found occurred near 150 keV, with the spectral index α changing from $1.74^{+0.05}_{-0.06}$ below the break to 2.3 ± 0.1 above it. Keeping the cutoff energies for PL1 and PL2 in Model 6 equal to each other, we found a lower limit of 400 keV to any break in the power-law. Future improvements to background modeling of the GSO may eventually allow us to establish more strict constraints.

3.2. *Hard X-ray emission lines and absorption edges*

In addition to that from Fe, fluorescent Kα lines from Si and S have been claimed by Sugizaki et al. (1997) and Evans et al. (2004). We added five more Gaussians, each with width tied to that of the Fe Kα line; it was significant at >90% confidence according to the F-test to add each line. The centroid energies are consistent with Kα emission from Si, S, Ca, Ar, and Ni; detection of the latter three lines are reported here for the first time. The decrease in χ^2 for each line, including the Fe Kα and Kβ lines, along with energy centroids, fluxes, and observed equivalent widths $EW_{\rm obs}$, are listed in Table 3. In the case of Si, we caution that, as data near 1.8 keV have been ignored due to calibration uncertainties, values of flux and equivalent width may be uncertain (e.g., some fraction of the large value of $\Delta\chi^2$ may be due to calibration uncertainties). The detection of the Ni line is robust: there does exist a Ni Kα line in the NEP background spectrum, but it is 200 times fainter than the source spectrum line. Data/model residuals to models with all six Kα lines and the Fe Kβ line removed are shown in Figures 7–9.

The Fe Kα line has a best-fit measured width of 14 eV, though formally the value is only an upper limit, 24 eV. The intrinsic width of the line is then found by subtracting in quadrature the ^{55}Fe calibration line width of 9^{+6}_{-2} eV from the measured line width. We infer an intrinsic line width of < 23 eV, which corresponds to a FWHM velocity of <2500 km s^{-1}.

We next explored the abundances of the hard X-ray absorbers (Model 7). The K-shell edges for Fe, Ca, and S are detected at >99.999% confidence, determined by setting each ZVPHABS abundance value to 0 and refitting.

The detection of the Ca K edge is likely robust: the response of a line at 6.4 keV includes a Si escape feature near 4.5 keV, but it is a factor of more than 50 fainter than the continuum and likely does not influence the Ca edge. The intrinsically weak Ar K and Ni K edges are not detected at high confidence; in the latter case, the decrease in the effective area of the XIS above 8 keV is also a factor. We re-fit the data, allowing $Z_{\rm Fe}$, $Z_{\rm Ca}$ and $Z_{\rm S}$ to vary, and keeping the abundances of all three absorbers tied to each other for simplicity. We also kept all other abundances fixed at solar. Best-fit model parameters for Model 7 are listed in Table 2; the edges are also displayed in Figures 7–9. The abundance results are listed in Table 4; note that the Fe abundance is inconsistent with solar at 3σ confidence. Given the column density of the absorbing material and the 2-3 keV rollover, most of the rollover is the result of absorption by K-shell O (with some contributions to the total opacity from K-shell Ne and L-shell Fe). We are thus actually measuring abundances relative primarily to O, not to H. The abundances listed relative to H in Table 4 implicitly assume $Z_{\rm O} = 1.0$.

To find the equivalent optical depth for each edge, we re-fit the data with $Z_{\rm Fe}$, $Z_{\rm Ca}$ and $Z_{\rm S}$ set to zero in the ZVPHABS components, but with edges at the appropriate energies. The results, listed in Table 4, show that the energy of each edge is consistent with absorption by neutral atoms.

The Fe Kβ/Kα intensity ratio can yield insight into the ionization state of the line-emitting gas. However, in the present spectrum, the Kβ line is somewhat blended with the Fe K edge. However, we note that the Fe K edge energy and depth are robust to the properties of the Kβ line, and the energy can be used to constrain the ionization state of the material, as discussed further in §4.

We searched for any possible Compton shoulder to the Fe Kα line by adding a Gaussian near 6.24 keV, but there was no improvement in the fit. We find an upper limit of 1.7×10^{-5} ph cm^{-2} s^{-1} to Compton shoulder emission (*EW* < 10 eV, determined relative to a locally-fit continuum).

Grandi et al. (2003) claimed emission due to ionized Fe near 6.8 keV using *BeppoSAX*. We added a narrow Gaussian at the rest energies of Fe XXV and Fe XXVI, with no change in the fit statistic in either case; upper limits to the *EW* of emission lines were 3 and 1 eV, respectively.

3.3. *Abundances of the thermal plasma*

We next explored the abundances, Z, of the thermal plasma relative to solar values. Abundances for the VAPEC1 and VAPEC2 components were kept tied to each other. We thawed one element at a time from solar, while assuming solar abundances for all other elements. Abundances relative to H can be measured accurately if the continuum is well-determined and the thermal emission is not too heavily dominated by lines. Given the presence of PL3, one must keep in mind that there could be systematic effects associated with some derived abundance values.

We did not find any strong evidence for non-solar abundances for C, N or O. The best chance to constrain $Z_{\rm C}$ in our model is via the C VI Ly α and Ly β lines at 0.368 and 0.436 keV, respectively. However, there are very few counts at these energies, and the PL3 component domi-

nates at these energies. Similarly, Z_N could, in principle, be constrained via the N VII Lyα line, but the line is not robustly detected. Allowing Z_O to vary resulted in a best-fit value of 0.95±0.35 solar, with χ^2 decreasing by only 1.7. We assume Z_C, Z_N and Z_O are solar for the rest of the paper.

We did not test the Si abundance: Si XIII emission cannot be constrained, as we have ignored data near the Si K instrument edge. The best-fit model does predict a modest Si XIV emission line at 2.05 keV, but at that energy, the PL3 component and the absorbed hard X-ray power-laws dominate.

In addition to Fe XVII emission lines, Fe is also responsible for a large bump in the continuum emission from about 0.7 to 1.0 keV. Adjusting the Fe abundance causes the PL3 component to vary in normalization to compensate, creating systematic uncertainty to Z_{Fe} derived from L-shell emission. We henceforth rely on the abundance determined using the K edge depth (§3.3).

We did, however, find significant improvements to the fit when the Ne or Mg abundances were varied. In the case of Ne, the best-fit abundance was $2.7^{+0.3}_{-0.2}$ solar; χ^2 decreased by 71 (F-test probability 2×10^{-15}). For Mg, the best-fit abundance was 1.6±0.3 solar, with χ^2 decreasing by 19 (F-test probability 2×10^{-5}).

We re-fit the data with the Ne and Mg abundances in VAPEC1 and VAPEC2 thawed (Model 8). We left the VAPEC abundances for C, N, O, Si and Fe fixed at solar (fixing Z_{Fe} at 1.17, the value derived from the Fe K edge, had minimal impact). In the best-fit model, Z_{Ne} and Z_{Mg} were 2.7±0.3, and 1.9±0.4, respectively. The temperature of the VAPEC2 component fell slightly to $0.56^{+0.01}_{-0.03}$ keV. With the exception of these parameters, all other previously-derived parameters did not change significantly compared to Model 7. The best-fit parameters for Model 8 are listed in Table 2. A contour plot of N_{H1} versus the photon index and normalization of the primary power-law is shown in Figure 10. An unfolded model spectrum in plotted in Figure 11.

3.4. *Continuum variability*

Having decomposed the broadband spectrum, it is natural to ask whether the observed 2–10 keV variability (see Figure 1) is due to variations in the flux of PL1, PL2, or both. Figure 12 shows the 2–4 and 5–10 keV light curves, summed over all 4 XISes and normalized by their respective means; the 2–4 keV band is dominated by PL1; PL3, a component which is not expected to display short-term variability, is an average factor of 30 times fainter in this band. In the 5–10 keV band, PL1 is a factor of roughly 6 times brighter than PL2. Fractional variability amplitudes for these two bands are similar: $F_{var,2-4} = 3.0 \pm 0.2\%$ and $F_{var,5-10} = 3.5 \pm 0.1\%$. Moreover, one can see that the two mean-normalized light curves display virtually identical variability trends.

The fact that the 2–4 keV band varies implies that PL1 does vary in flux. If PL2 is constant or only negligibly variable, then variability in the 5–10 keV should be diluted relative to that in the 2–4 keV band[16]. However,

it is not the case that $F_{var,5-10}$ is significantly lower than $F_{var,2-4}$; in fact, $F_{var,5-10}$ is slightly higher than $F_{var,2-4}$. On the other hand, with such small F_{var} values and the fact that PL1 is so much brighter than PL2, it is difficult to accurately conclude anything about whether PL2 is constant, as variable, or more variable than PL1.

While we have confirmed that PL1 varies, the similarity in F_{var} for both bands and the similarity in variability trends means we cannot rule out the idea that both PL1 and PL2 vary in concert, as expected if a partial covering scenario applies. Further progress can be made through continued broadband monitoring spanning a larger flux range.

4. DISCUSSION

The broad bandpass of the XIS and HXD aboard *Suzaku* has allowed us to obtain a high-quality spectrum spanning nearly 3 decades in photon energy. The long exposure time, narrow response, and the low background make the XIS spectrum one of the highest quality CCD spectra of Cen A to date, particularly below 2 keV.

In §4.1, we compare our results to other recent works to test for evidence of long-term variations in several observed parameters. The dual power-laws which dominate the hard X-rays, and the material which absorbs them, are both discussed in §4.2. That same absorbing material is likely the origin of the fluorescent emission lines; the nature of the Fe Kα line is discussed in §4.3. The soft X-ray emission from the thermal plasma is discussed in §4.4. Finally, in §4.5, element abundances are derived from the hard X-ray absorption edges and fluorescent emission lines, the first time abundances in the absorbing gas of Cen A have been measured. In conjunction with abundances measured using the thermal plasma lines, we show that the abundances are consistent with enrichment from star formation.

4.1. *Comparison to previous observations*

We can compare our results to previous works to search for any variations in flux, photon index, column densities, and Fe Kα line flux.

We find an absorbed 2–10 keV flux of 2.12×10^{-10} erg cm^{-2} s^{-1}, similar to values obtained by Rothschild et al. (2006) for *RXTE* and *INTEGRAL* observations of Cen A between 2003 and 2004. We find a 20–100 keV flux of 6.4×10^{-10} erg cm^{-2} s^{-1}, within the range of 20–100 keV fluxes measured by Rothschild et al. (2006). We measure a unabsorbed 4–7 keV continuum flux of 1.5×10^{-10} erg cm^{-2} s^{-1} and a 2–10 keV absorbed luminosity of 2.9×10^{41} erg s^{-1}, values almost identical to those found by Evans et al. (2004) during the 2001 *XMM-Newton* observation. These facts suggest the source has not varied in hard X-ray flux greatly over the last five years.

The photon index, power-law normalization, and absorbing column density of the primary (brighter) power-law, PL1, are all similar to values obtained by Rothschild et al. (2006). Evans et al. (2004), modeling *XMM-Newton* observations in 2001 and 2002 and a *Chandra* observation in 2002, fit partial-covering models ($\Gamma_1=\Gamma_2$) and dual

---

[16] If a lightcurve C consists of a variable component A plus a constant component B, then $F_{var}(C)$ will be equal to $F_{var}(A)/(1 + \frac{\mu_B}{\mu_A})$, where μ_A and μ_B are the average count rates of lightcurves A and B, respectively. For instance, if PL1 is an average of 6 times brighter than PL2 in the 5–10 keV band, and PL2 is constant, than $F_{var,5-10}$ should be $6/7 \times F_{var}(PL1)$ (assuming emission from PL3 is negligible).

power-law models (Γ_2 not tied to Γ_1). In all previous observations, the parameters of the primary power-law and its absorber are very similar to those for the *Suzaku* observation, suggesting a lack of strong variations over the last five years.

The $EW_{\rm obs}$ of the Fe Kα line in the *Suzaku* observation is consistent with that measured from the *XMM-Newton* observations; we measure the Fe Kα line intensity to be $2.32 \pm 0.1 \times 10^{-4}$ ph cm^{-2} s^{-1}; the unabsorbed Fe Kα flux of 2.6×10^{-12} erg cm^{-2} s^{-1}, consistent with the *Chandra* and 2001 *XMM-Newton* observations (Evans et al. 2004). Our $EW_{\rm obs}$ values for the Si and S lines are consistent with those obtained using *Chandra*-HETGS. The *Suzaku* observation thus shows no evidence for variability of the Fe, Si or S Kα lines compared to the 2001–2002 observations.

4.2. *Continuum emission components*

We now turn our attention to the nature of the two hard X-ray power-laws, PL1 and PL2, and the less-absorbed, soft X-ray power-law PL3. The absorbers for PL1 and PL2 are similar in column density to absorbers seen in some other radio galaxies (Wozniak et al. 1998). Cen A's dust lane provides an optical extinction of 3–6 mag, which, assuming a Galactic gas/dust ratio, corresponds to a column $N_{\rm H} \sim 5\text{--}10 \times 10^{21}$ cm^{-2}. The circumnuclear material within a few hundred pc of the black hole, however, is believed to have a much higher column, $\sim 10^{23}$ cm^{-2}. Both hard X-ray absorbers are thus more likely associated with the circumnuclear material than the optical dust lane; PL3, meanwhile, is consistent with absorption by the optical dust lane only.

Historically, it has not been clear whether the X-ray emission is associated with jet or accretion processes. As far as jet emission is concerned, several papers in the 1980s (e.g., Burns et al. 1983) suggested that the X-ray emission was synchrotron emission. However, by constructing the broadband SED, Chiaberge et al. (2001) concluded that the X-ray continuum was primarily inverse Compton emission, with the synchrotron component peaking in the far-IR and falling by 10^{15-16} Hz. We can gauge if one or more of the three power-laws observed by *Suzaku* are consistent with X-ray emission from a jet by using the radio–X-ray luminosity density correlations of Canosa et al. (1999) and Evans et al. (2006), which are based on samples of low-redshift radio galaxies. The total 5 GHz luminosity density of the nucleus of Cen A is $\sim 6 \times 10^{20}$ W Hz^{-1} sr^{-1} (e.g., Evans et al. 2006). This value corresponds to a 1 keV luminosity density of $\sim 1\text{--}2 \times 10^{14}$ W Hz^{-1} sr^{-1}. The 1 keV power-law normalizations for PL1, PL2 and PL3 correspond to, respectively, 1 keV flux densities of 70, 12 and 0.4 μJy, or 1 keV luminosity densities of $\sim 8 \times 10^{15}$, 1×10^{15}, and 4×10^{13} W Hz^{-1} sr^{-1}. It is therefore plausible that PL3 could correspond to jet emission. The X-ray luminosity density of PL2 places it an order of magnitude above the Canosa et al. (1999) and Evans et al. (2006) relations; however, given that there is roughly an order of magnitude of scatter in the relations, it is still possible that PL2 could be associated with jet emission,

We can now revisit previous suggestions that there could exist two physically distinct sites of hard X-ray continuum emission. Our best-fit model indicates components with unabsorbed 2–10 keV luminosities of 6.7×10^{41} erg s^{-1} (PL1) and 1.3×10^{41} erg s^{-1} (PL2), each independently absorbed by different columns. Evans et al. (2004) suggested that the primary power-law, PL1, arises via Bondi accretion onto the black hole, consistent with the low accretion rate of Cen A (0.2% of Eddington), and consistent with PL1 representing X-ray emission far in excess above what is expected from jet emission. Evans et al. (2004) also suggested that their secondary power-law component could be associated with X-ray emission from the pc-scale jet. Our PL2 component has a 1 keV normalization $\gtrsim 3$ times higher and an absorbing column density a factor of $\gtrsim 10$ higher compared to the secondary power-law component detected by Evans et al. (2004). However, a one-to-one correspondence between our PL2 and the *Chandra/XMM-Newton* secondary power-law is highly uncertain. We are using larger PSFs and extraction radii than Evans et al. (2004); the secondary power-law component detected by Evans et al. (2004) could be overwhelmed by non-nuclear emission (e.g., what we detect as PL3) in the *Suzaku* spectrum. Meanwhile, *Chandra*-HETGS's low effective area > 5 keV makes it relatively insensitive to the presence of a power-law component absorbed by a column 7×10^{23} cm^{-2}. It is therefore possible, though not certain, that PL2 could correspond to X-ray emission associated with the pc-scale jet. In the soft X-rays, PL3 could be the sum of diffuse X-ray emission and knots within the kpc scale jet, scattered nuclear emission, and emission from other point sources resolved by *Chandra*-ACIS. The 0.5–3 keV luminosity of PL3 is 1×10^{40} erg s^{-1}, similar to the sum of the jet and knot component luminosities as reported by Kraft et al. (2002) and Kataoka et al. (2006). PL3 may additionally reflect uncertainties in modeling the thermal gas.

Alternatively, as suggested by Turner et al. (1997), a partial-covering model, with only one site of hard X-ray emission, is applicable, as the photon indices of PL1 and PL2 are consistent. Our best-fit model is consistent with the idea that the central hard X-ray source is powered by accretion. 84% of the sky as seen from the central hard X-ray source is covered by a column 1.5×10^{23} cm^{-2}, and the remaining 16% by a column 7×10^{23} cm^{-2}. In this model, PL3 represents the sum of X-ray emission from both the kpc-scale and pc-scale jets, any scattered nuclear emission, jet knots, XRBs and other point sources, all modified by dust lane absorption, along with any uncertainty in modeling the thermal gas.

Finally, we comment on the absence of a strong Compton reflection component. The low R value could of course indicate the absence of a large amount of Compton-thick material which is brightly illuminated by the primary continuum and also efficiently radiates the reflection continuum. An alternate suggestion is that the Compton hump is diluted by a power-law component, e.g., from one of the jets. However, the large Fe line flux observed is inconsistent with this notion. In addition, Wozniak et al. (1998) demonstrated that spectral fitting of several radio galaxies which also displayed weak or non-existent Compton humps is inconsistent with this notion.

4.3. *The origin of the Fe Kα line*

Assuming that the line originates in gas which is in virialized orbit around the black hole, we can estimate the distance r from the black hole to the Fe Kα line-emitting

gas. The width of the Fe Kα line corresponds to a FWHM velocity $v_{\rm FWHM}$ of <2500 km s^{-1}. Assuming that the velocity dispersion is related to $v_{\rm FWHM}$ as $<v^2> = \frac{3}{4}v^2_{\rm FWHM}$ (Netzer et al. 1990), assuming a black hole mass $M_{\rm BH}$ of 2×10^8 M$_\odot$, and using $GM_{\rm BH} = rv^2$, we find a lower limit to r of 6×10^{15} m = 200 light-days. The best-fit edge energy, 7.103±0.015 keV, is consistent with absorption by Fe I, though ionization stages up to Fe $\sim$V cannot be ruled out (Kallman et al. 2004).

It is plausible that the same material that absorbs the hard X-rays is responsible for producing the fluorescent lines. The fact that no Compton hump or 6.2 keV Compton shoulder are seen, indicating an origin for the Fe Kα line in Compton-thin material, supports this notion. On the other hand, the material cannot have a column substantially less than $10^{\sim22}$ cm^{-2} or else there would be insufficient optical depth to produce a prominent Fe K line. As an estimate of the Fe Kα equivalent width expected in this case, we can use the following equation:

$$EW_{\rm calc} = f_{\rm c}\omega f_{\rm K\alpha}A\frac{\int_{E_{\rm Kedge}}^{\infty} P(E)\sigma_{\rm ph}(E)N_{\rm H}dE}{P(E_{\rm line})} \quad (1)$$

This method assumes an origin in optically-thin gas which completely surrounds a single X-ray continuum source and is uniform in column density. Emission is assumed to be isotropic. Here, $f_{\rm c}$ is the covering fraction, initially assumed to be 1.0. ω is the fluorescent yield: the value for Fe, 0.34, was taken from Kallman et al. (2004). $f_{\rm K\alpha}$ is the fraction of photons that go into the Kα line as opposed to the Kβ line; this is 0.89 for Fe I. A is the number abundance relative to hydrogen. Initially, we assumed solar abundances, using Lodders (2003). $P(E)$ is the spectrum of the illuminating continuum at energy E; $E_{\rm line}$ is the Kα emission line energy. The illuminating continuum is assumed to be the sum of both unabsorbed hard X-ray power-laws in Cen A, as $EW_{\rm obs}$ values were determined relative to the total, local continuum. We note that the fainter power-law component cannot reproduce the entire Fe line as $EW_{\rm obs}$ is too large; the primary power-law must be responsible for the bulk of the line. $\sigma_{\rm ph}(E)$ is the photo-ionization cross section assuming absorption by K-shell electrons only; all cross sections were taken from Veigele (1973[17]). $N_{\rm H}$ is the column density. The two hard X-ray absorbing components in Model 8 have column densities 1.5 and 7×10^{23} cm^{-2}, which attenuate power-laws with normalizations in a 5.3:1 ratio. We therefore use an weighted average $N_{\rm H}$ column of 2.2×10^{23} cm^{-2}. (Strictly speaking, the observation in Cen A of two different column densities argues against the use of a single, uniform column; however, this weighted average suffices for our purpose of estimating the total Fe Kα EW expected from both absorbers.)

The value of $EW_{\rm calc}$ is 128 eV, a factor of 1.5 higher than $EW_{\rm obs}$. Assuming that $Z_{\rm Fe} = 1.17$, as the Fe K absorption edge depth suggests, yields $EW_{\rm calc} = 153$ eV. Possible explanations for this discrepancy include: 1) The initial assumption of a 100% covering fraction for the line-emitting gas may be incorrect. Assuming isotropic emission, $f_{\rm c} = 0.7$ ($Z_{\rm Fe} = 1.0$) or 0.6 ($Z_{\rm Fe}$=1.17) may fit the data. Such values would be more consistent with an origin in a disk as opposed to a shell completely surrounding

the core. 2) The illuminating X-ray continuum may be anisotropic. For instance, Rothschild et al. (2006) found that $I_{\rm K\alpha}$ was not correlated with $N_{\rm H}$ and suggested that the line-emitting gas may lie along the VLBI jet some distance from the black hole. 3) The line-emitting gas may be responding to an illuminating flux which is $\sim$0.6 of the observed flux. This is possible, for instance, if the line-emitting gas is $\gtrsim$200 light-days from the X-ray continuum origin, and does not lie on our line of sight to the continuum origin; the observed line flux is a response to the continuum flux convolved with a >200-day time delay. *Swift*/BAT monitoring indicates that the average 14–195 keV flux of Cen A in early 2005 was very roughly 15% higher compared to the flux in August 2005 (*Swift* team, priv. comm.[18]), possibly explaining some of the line flux discrepancy. Continued long-term monitoring of the continuum and line fluxes may shed light on this issue. Alternatively, the line of sight from the continuum origin to the line-emitting gas may be blocked, by a clump of gas which absorbs 40% of the >7 keV flux and which does not lie along our line of sight to the continuum. 4) It is plausible that our initial assumption of a uniform-column density absorber is incorrect and the absorbers are instead clumpy; this is more consistent with the observation of two different columns. There could be higher columns lying out of our line of sight to the X-ray continuum source. For instance, we can use Eq. 1 of Wozniak et al. (1998), which gives the expected Fe Kα intensity assuming a cloud with a column $\gtrsim 10^{23}$ cm^{-2} lying off the line of sight and subtending a fraction $\Omega/4\pi$ of the sky as seen from the source, as a function of the K edge optical depth and the spectral index and normalization of the illuminating continuum. We find a solid angle of $\Omega/4\pi \sim$ 0.5 yields a predicted line intensity compatible with what *Suzaku* observes. Such a covering fraction suggests a torus or some sort of infinite slab, e.g., a disk-like structure, though the current data cannot constrain whether such a disk would be in the form of a "standard" optically-thick, geometrically-thin disk at all radii or a "disk + sphere" hybrid (e.g., Esin, McClintock & Narayan 1997), wherein the inner parts of a standard thin disk are replaced by a radiatively-inefficient flow such as an advection dominated accretion flow (Narayan & Yi 1995).

4.4. Soft X-ray emission from the thermal plasma

The *Suzaku* XIS has yielded the best soft X-ray spectrum obtained to date for Cen A, revealing emission lines which likely originate in the thermal plasma that extends from the nucleus to a radius of $\sim$6 kpc. At least the inner parts of the gas are likely heated by the AGN central engine and/or the nuclear starburst; O'Sullivan, Ponman & Collins (2003) demonstrated that the gas in the central 2 kpc of Cen A has a much higher temperature then the >2 to 14 kpc gas in the halo.

Photo-ionization does not yield as good a fit to the *Suzaku* data as collisional ionization models, as the former cannot reproduce the strong observed Fe L emission complex. Specifically, to obtain a good model fit, we have assumed that the emission is entirely collisional in nature, and used a two-temperature VAPEC model, with $k_{\rm B}T$

---

[17] http://www.pa.uky.edu/~verner/photo.html

[18] See also the *Swift*/BAT Transient Monitoring web page, http://swift.gsfc.nasa.gov/docs/swift/results/transients/

near 0.2 and 0.6 keV. This is similar to results obtained in a wide variety of spiral and starburst galaxies (see references in Strickland et al. 2004). However, we are likely sampling thermal emission from plasma spanning a range of temperatures. For example, the soft X-rays are likely not completely dominated by emission from gas with $k_B T$ above 0.6 keV, or else we would detect a H-like Mg line at least as intense as the He-like Mg line, and the He-like Ne line would be extremely faint. Similarly, emission from gas with $k_B T < 0.20$ keV does not dominate, as the Ne X would be extremely faint.

4.5. *Constraints on abundances*

We have derived estimates of Z_S, Z_{Ca} and Z_{Fe} using the K shell edge depths, and estimates of Z_O, Z_{Ne}, and Z_{Mg} from the thermal plasma (for the remainder of this paper, we assume that the abundances in the extended thermal plasma and in the circumnuclear absorbing material are identical).

We can also estimate abundances relative to Fe, e.g., Z_{Si}/Z_{Fe}, from the Kα fluorescent lines and Eq. 1. Values of ω were taken from the X-ray Data Booklet[19]. For Ni and Ca, $f_{K\alpha} = 0.89$ and 0.88, respectively, assuming neutral atoms (Bambynek et al. 1972). We assume $f_{K\alpha} = 0.9$ for all other elements. The values of EW_{calc}, calculated assuming solar abundances and a covering fraction f_c=1.0, are listed in Table 3.

Relative abundances are calculated as, e.g., $Z_{Si}/Z_{Fe} = (EW_{obs,Si}/EW_{calc,Si}) / (EW_{obs,Fe}/EW_{calc,Fe})$, where $EW_{calc,Fe}$ has been estimated using the abundance derived from the Fe K edge depth, Z_{Fe}=1.17, and the solar abundance was used for $EW_{calc,Si}$. We caution that for Ar, Ca, and Ni, the lines are weak and the statistics are poor. For Si, there may be systematic effects due to current XIS calibration as well as from the fact that the continuum near 1.7 keV is mixture of all three power-law components. Table 5 lists the abundance ratios. There is agreement on the values of Z_S/Z_{Fe} derived from the edges and from the lines.

We observe [m/H] = $\log(Z_{Fe})$ = +0.1, a slightly higher metallicity value than in the metal-rich population of globular clusters at 2–20 kpc radii ([m/H] $\sim$ −0.1, Peng et al. 2004) or in the outer stellar bulge component (e.g., [m/H] $\sim$ –0.2 at a radius of 8 kpc, Harris & Harris 2002). It is only slightly higher than values for the ISM of other early-type galaxies (Humphrey & Buote 2006). Our observed value of Z_{Mg}/Z_{Fe} is consistent with the value of 2 obtained by Peng et al. (2004) for Cen A's globular clusters. It is similar to values for the stellar components of large ellipticals in general, [m/H] $\sim$ 0.0 − 0.4 (Henry & Worthey 1999). Trager et al. (2000) also found the stellar populations of 8 field ellipticals to have [m/H] $\sim$ 0.0−0.4, though it may not be straightforward to compare Cen A to field ellipticals due to Cen A's recent merger.

However, our observed [m/H] value is much higher than the average value found in the halo stars of Cen A, [m/H] = –0.4 at radii of 20–30 kpc (Harris & Harris 2000, Harris, Harris & Poole 1999). It is therefore unlikely that the circumnuclear material and the diffuse plasma have directly originated in the relatively metal-poor outer halo, unless enrichment via local star formation has occurred.

[19] http://xdb.lbl.gov

The pre-merger origin of the circumnuclear material cannot be known for certain, though it is plausible that during the merger, gaseous material originally in the outer portions of the progenitor galaxies lost sufficient angular momentum to be transported to the nuclear regions (Toomre & Toomre 1972). Furthermore, connections between the nuclear gas and starburst activity at radii of hundreds of pc and less are well-known (e.g., Hopkins et al. 2006 and references therein). The likelihood that Cen A's circumnuclear gas has been enriched due to starburst processes is therefore high.

The degree of metallicity enrichment depends on many factors, including the IMF, star formation rate, and the total gas consumed, but simulations of disk-disk mergers incorporating star formation by Mihos & Hernquist (1994) demonstrated that [m/H] values of 0.3–0.4 at the center of the resulting merged ellipticals are plausible. The metallicity value derived from the *Suzaku* data is consistent with enrichment due to the ongoing star formation in the inner bulge, as a result of the merging process.

The observed relative element abundances also support enrichment. We calculated the expected relative abundances due to enrichment by Type II and Type Ia SNe, ignoring enrichment via stellar wind processes. We used the abundances relative to solar as found in Tsujimoto et al. (1995; their Figures 1–2), assuming a Salpeter IMF, converting to the abundances of Lodders (2003), and assuming one Type Ia explosion for every ten Type II explosions. For the ratios listed in Table 5, we expect Z_O/Z_{Fe} $\sim$2.5, Z_{Ne}/Z_{Fe} through Z_{Si}/Z_{Fe} to be 1.4–1.7, and Z_S/Z_{Fe} through Z_{Ca}/Z_{Fe} and Z_{Ni}/Z_{Fe} to all be $\sim$ 0.7–0.9. Most of our observed abundance ratios are consistent (or at least roughly consistent) with these predictions. The current burst of star formation is estimated to have started at least 50 Myr ago (e.g., Dufour et al. 1979). Assuming star formation at a uniform rate of 30 M$_\odot$ yr^{-1} (Telesco 1978 measured a star formation rate ten times that of the Milky Way's spiral arms), this is sufficient to enrich the gas to the current metallicity levels within that time span (M. Loewenstein, priv. comm.), although we cannot know for certain how much enrichment of the gas has occurred within the last 10^8 yr and how much occurred closer in time to the merger.

Finally, we discuss the argument of Hardcastle, Evans and Croston (2007) that "high-excitation" sources, which have torus-like circumnuclear absorbing gas and which accrete at moderate fractions of the Eddington limit (e.g., FR IIs), are fueled by a supply of cold gas, i.e., gas transported to the nucleus as a result of a merger or tidal interactions. In contrast, "low-excitation" sources, which include all FR I's and some of the less powerful FR IIs, may be powered by accretion of hot (X-ray emitting) gas. As mentioned before, Cen A, though classified as an FR I, has heavy X-ray absorption characteristic of most FR IIs. Our observation of high metallicity, indicative of cold gas being transported inwards to the nucleus as a result of the merger, is thus consistent with this argument of "cold-mode" accretion.

5. CONCLUSIONS

The combination of *Suzaku*'s XIS and HXD has allowed us to obtain a high quality spectrum of the nucleus (inner 2 kpc) of Cen A spanning 0.3–250 keV. The long exposure time, narrow response of the XIS, and the low background make the XIS spectrum one of the highest quality CCD spectra of Cen A to date, particularly below 2 keV. The HXD-PIN above 12 keV is more sensitive than *RXTE*-HEXTE or *INTEGRAL* instruments, allowing us to accurately and directly measure the 12–76 keV flux and spectral shape. The HXD-GSO provides a direct estimate of the 45–250 keV flux of Cen A.

Our best-fit model includes several broadband components. The >3 keV emission can be fit by two absorbed power-laws. The primary (brighter) power-law is absorbed by a column of about 1.5×10^{23} cm^2. The secondary power-law, with a brightness about 19% of the primary, is absorbed by a much higher column, about 7×10^{23} cm^2. In our best-fit model, the photon indices were the same, and the best-fit value was $1.817^{+0.023}_{-0.010}$. Untying the photon indices did not result in a significant fit improvement. Including data down to 0.3 keV, we find that two VAPEC components plus a third absorbed power-law component can fit the data. The soft X-rays reveal emission lines due to He- and H-like O, Fe XVII, He- and H-like Ne, and He-like Mg. The strong Fe L emission supports an origin in collisionally-ionized, rather than photo-ionized, gas. Two VAPEC components of temperatures $k_B T = 0.2$ and 0.6 keV can model the soft X-ray emission lines well.

The *Suzaku* data are consistent with scenarios previously forwarded to explain the nature of the various power-law components. As suggested by Evans et al. (2004), the primary, hard X-ray power-law is likely associated with Bondi accretion at the black hole. The secondary power-law could represent X-ray emission associated with the pc-scale VLBI jet, though this is not certain. Alternatively, a partial covering model, as suggested by Turner et al. (1997), may apply: 84% (16%) of the sky as seen from the X-ray source is obscured by a column 1.5 (7) $\times 10^{23}$ cm^2. In any event, it more likely that the material obscuring the hard X-rays is associated with the circumnuclear material than with the optical dust lane. The third, soft X-ray power-law component is consistent with absorption by the optical dust lane only. It likely represents a blend of diffuse emission and knot emission from the kpc-scale jet (as well as possibly the pc-scale jet), plus emission from a population of XRBs and other X-ray point sources, plus a likely contribution from scattered nuclear emission, which is likely less than 1% of the total hard X-ray power-law emission.

The hard X-ray photon index, the 2–10 keV flux, the Fe Kα line intensity and the column density of the material absorbing the primary power-law are all consistent with recent observations over the last ∼5 years, suggesting that no large variations in these parameters have occurred over the last few years. During the *Suzaku* observation, the hard X-ray flux was not strongly variable on short timescales, showing only a 10% increase in flux throughout the observation.

K-shell absorption edges due to Fe, Ca, and S are significantly detected. Several fluorescent emission lines, likely originating in the absorbing material, are detected. In addition to Fe Kα and Fe Kβ, Kα lines from Si, S, Ar, Ca and Ni are detected at at least 90% confidence. The latter three are detected for the first time in Cen A. The strict upper limit on the amount of Compton reflection, $R < 0.05$, supports the notion that the fluorescent lines originate in Compton-thin material. The Fe Kα line width is < 2500 km s^{-1} FWHM. If the line-emitting material is in virial orbit, then it is no closer than 200 light-days to the black hole. No emission due to He- or H-like Fe is detected. The Fe K edge energy is consistent with absorption by Fe I; ionization stages above Fe ∼V are ruled out. The gas does not likely completely surround the X-ray continuum source; the equivalent width of the Fe Kα line is more consistent with gas which is clumpy and/or covers the continuum source only partially, or the bulk of the gas may lie off the line of sight to the X-ray source, possibly in the form of a disk.

Metallicities are measured for the circumnuclear absorbing gas for the first time in Cen A. The high signal-to-noise ratio of the XIS spectrum has enabled us to use the K-shell absorption edge depths, relative fluorescent line strengths, and thermal plasma emission lines to derive abundances (we have assumed abundances in the thermal plasma gas are same as those for the circumnuclear absorbing material). We observe a value of $[m/H] = \log(Z_{Fe}) = +0.1$ for the circumnuclear material/diffuse plasma which is much higher than for the halo stars at 20–30 kpc radii. It is likely that the merger which created Cen A's famous edge-on dust disk also triggered the infall of cold gas into the inner regions of Cen A, where it currently accretes onto the black hole. Our metallicity observation suggests that the accreting material could not have originated in the relatively metal-poor outer halo unless enrichment due to local star formation occurred at some point. The relative observed abundances are indeed consistent with enrichment by a mixture of Type II and Type Ia supernovae.

This high signal-to-noise ratio CCD observation has yielded breakthroughs in constraining abundances, but further progress can be made with a very high-spectral resolution instrument, such as the planned calorimeter aboard *Constellation-X*. By better constraining the widths and intensities of Kα emission lines and soft X-ray emission lines, as well as edge energies and depths, *Constellation-X* will thus yield abundance constraints on the circumnuclear material in potentially many dozens of AGNs once it is launched.

REFERENCES

Bailey, J., Sparks, W.B., Hough, J.H., Axon, D.J. 1986, Nature, 322, 150

Balmaverde, B., Capetti, A. & Grandi, P. 2006, A&A, 451, 35

Bambynek, W., Crasemann, B., Fink, R., Freund, H.-U., Mark, H., Swift, C., Price, R. & Rao, P.V. 1972, Rev. Mod. Phys. 44, 716

Benlloch, S., Rothschild, R., Wilms, J., Reynolds, C.S., Heindl, W.A. & Staubert, R. 2001, A&A, 371, 858

Canosa, C.M., Worrall, D.M., Hardcastle, M.J. & Birkinshaw, M. 1999, MNRAS, 310, 30

Chiaberge, M., Capetti, A. & Celotti, A. 2001, MNRAS, 324, L33

Donato, D., Sambruna, R. & Gliozzi, M. 2004, ApJ, 617, 915

Dufour, R.J., Harvel, C.A., Martins, D.M., Schiffer, F.H.,III, Talent, D.L., Wells, D.C., van den Bergh, S. & Talbot, R.J., Jr. 1979, AJ, 84, 284

Ebneter, K. & Balick, B. 1983, PASP, 95, 675

Esin, A., McClintock, J. & Narayan R., 1997, ApJ, 489, 865

Evans, D.A., Kraft, R.P., Worrall, D.M., Hardcastle, M.J., Jones, C., Forman, W.R., & Murray, S.S. 2004, ApJ, 612, 786

Evans, D.A., Worrall, D.M., Hardcastle, M.J., Kraft, R.P. & Birkinshaw, M. 2006, ApJ, 642, 96

Feigelson, E.D., Schreier, E.J., Delvaille, J.P. Giacconi, R., Grindlay, J.E. & Lightman, A.P. 1981, ApJ, 251, 31

Fujimoto, R. et al. 2007, PASJ, in press

Fukazawa, Y. et al. 2007, Suzaku Memo 2007-02

Graham, J.A. 1978, PASP, 90, 237

Grandi, P. et al. 2003, ApJ, 593, 160

Gruber, D.E., Matteson, J.L., Peterson, L.E. & Jung, G.V. 1999, ApJ, 520, 124

Hardcastle, M.J., Evans, D.A. & Croston, J.H. 2007, MNRAS, in press (astro-ph/0701857)

Harris, G.L.H., Harris, W.E. & Poole, G. 1999, AJ 117, 885

Harris, G.L.H. & Harris, W.E. 2000, AJ, 120, 2423

Harris, W.E. & Harris, G.L.H. 2002, AJ, 123, 3108

Henry, R.B.C. & Worthey, G. 1999, PASP, 111, 919

Hopkins, P.F., Hernquist, L., Cox, T.J., Di Matteo, T., Robertson, B. & Springel, V. 2006 ApJS, 163, 1

Humphrey, P.J. & Buote, D.A. 2006 ApJ, 639, 136

Ishisaki, Y. et al. 2007, PASJ, in press (astro-ph/0610118)

Israel, F.P. 1998, A&A Rev., 8, 237

Kallman, T.R., Palmeri, P., Bautista, M.A., Mendoza, C. & Krolik, J.H. 2004, ApJS, 155, 675

Karovska, M., Marengo, M., Elvis, M., Fazio, G., Hora, J., Hinz, P., Hoffmann, W., Meyer, M. Mamajek, E. 2003, ApJ, 598, L91

Kataoka, J., Stawarz, L., Aharonian, F., Takahara, F., Ostrowksi, M. & Edwards, P.G. 2006, ApJ, 641, 158

Kinzer, R.L. et al. 1995, ApJ, 449, 105

Kokubun, M. et al. 2007, PASJ, in press

Koyama, K. et al. 2007, PASJ, in press

Kraft, R.P. et al. 2000, ApJ, 531, L9

Kraft, R.P., Forman, W.R., Jones, C., Murray, S.S., Hardcastle, M.J. & Worrall, D.M. 2002, ApJ, 569, 54

Lodders, K. 2003, ApJ, 591, 1220

Makashima, M. 1986, in The Physics of Accretion onto Compact Objects, eds. K. Mason, M. Watson & N. White (Berlin: Springer-Verlag), 249

Matt, G. 2002, MNRAS, 337, 147

Mihos, J.C. & Hernquist, L. 1994, ApJ, 427, 112

Mitsuda, K. et al. 2007, PASJ, in press

Mushotzky, R.F., Serlemitsos, P.J., Boldt, E.A., Holt, S.S. & Becker, R.H. 1978, ApJ, 220, 790

Narayan, R. & Yi, I. 1995, ApJ, 444, 231

Netzer, H. et al. 1990, ApJ, 353, 108

O'Sullivan, E., Ponman, T.J. & Collins, R.S. 2003, MNRAS, 340, 1375

Peng, E.W., Ford, H.C. & Freeman, K.C. 2004, ApJ, 602, 705

Quillen, A.C., de Zeeuw, P.T., Phinney, E.S. & Phillips, T.G. 1992, ApJ, 391, 121

Rejkube, M. 2004, A&A, 413, 903

Rothschild, R. et al. 1999, ApJ, 510, 651

Rothschild, R., Wilms, J., Tomsick, J., Staubert, R., Benlloch, S., Collmar, W., Madejski, G., Deluit, S. & Khandrika, H. 2006, ApJ, 641, 801

Serlemitsos, P.J. et al. 2007, PASJ, in press

Schreier, E.J. et al. 1998, ApJ, 499, L143

Silge, J.D., Gebhardt, K., Bergmann, M. & Richstone, D. 2005, AJ, 130, 406

Steinle, H. et al. 1998, A&A, 330, 97

Strickland, D.K., Heckman, T., Colbert, E.J M., Hoopes, C.G. & Weaver, K.A., 2004, ApJS, 151, 193

Sugizaki, M., Inoue, H., Sonobe, T., Takahashi, T. & Yamamoto, Y. 1997, PASJ, 49, 59

Takahashi, T. et al. 2007, PASJ, in press

Telesco, C.M. 1978, ApJ, 226, L125

Tingay, S. et al. 1998, AJ, 115, 960

Toomre, A. & Toomre, J. 1972, ApJ, 178, 623

Trager, S.C., Faber, S.M., Worthey, G. & González, J.J. 2000, AJ, 120, 165

Tsujimoto, T., Nomoto, K., Yoshii, Y., Hashimoto, M., Yanagida, S., Thielemann, F.-K. 1995, MNRAS, 277, 945

Turner, T.J., George, I.M., Mushotzky, R.F. & Nandra, K. 1997, ApJ, 475, 118

Vaughan, S., Edelson, R., Warwick, R. & Uttley, P. 2003, MNRAS, 345, 1271

Veigele, W.M. 1973, Atomic Data Tables, 5, 51

Wozniak, P.R., Zdziarski, A.A., Smith, D., Madejski, G. & Johnson, W.N. 1998, MNRAS, 299, 449

Table 1
Soft X-ray Emission Lines

Line Identification	Observed Energy Centroid (keV)	Intensity (10^{-5} ph cm^{-2} s^{-1})	EW (eV)
O VII	$0.564^{+0.006}_{-0.004}$	10.9 ± 2.1	39 ± 0.8
O VIII	0.654 ± 0.003	$9.3^{+2.6}_{-1.1}$	37^{+10}_{-4}
Fe XVII 3s–2p ($^3P_1/^3P_2/^1P_1$)	$0.732^{+0.004}_{-0.006}$	$5.3^{+1.0}_{-0.7}$	23^{+4}_{-3}
Fe XVII 3d–2p ($^1P_1/^3D_1$)	$0.820^{+0.005}_{-0.003}$	$7.4^{+0.8}_{-1.4}$	33^{+4}_{-6}
Ne IX	0.901 ± 0.004	$6.3^{+0.6}_{-0.9}$	36^{+3}_{-5}
Ne X	1.010 ± 0.003	4.1 ± 0.6	33 ± 5
Mg XI	$1.331^{+0.008}_{-0.004}$	1.5 ± 0.4	22 ± 6

Note. — Equivalent widths EW (Col. [4]) were determined relative to a locally-fit continuum.

Table 2
Best-fit parameters for selected models

Parameter	Model 5	Model 6	Model 7	Model 8
χ^2/dof	9806.8/9158	9745.1/9159	9639.6/9144	9529.9/9142
$\Gamma_{1,2}$	$1.852^{+0.008}_{-0.019}$	$1.831^{+0.019}_{-0.010}$	$1.820^{+0.016}_{-0.010}$	$1.817^{+0.023}_{-0.010}$
PL1 Norm.[1]	$0.116^{+0.002}_{-0.012}$	0.112 ± 0.002	0.111 ± 0.002	$0.111^{+0.001}_{-0.002}$
$N_{\rm H,1}$ (/10^{22} cm^2)	$15.2^{+0.1}_{-0.6}$	15.1 ± 0.2	14.7 ± 0.2	$14.7^{+0.3}_{-0.2}$
PL2 Norm.[1]	$0.026^{+0.004}_{-0.002}$	0.022 ± 0.003	$0.021^{+0.002}_{-0.003}$	0.021 ± 0.003
$N_{\rm H,2}$ (/10^{22} cm^2)	82 ± 7	75 ± 8	72^{+10}_{-3}	70^{+11}_{-7}
VAPEC1 $k_{\rm B}T$ (keV)	$0.31^{+0.03}_{-0.02}$	0.24 ± 0.02	0.23 ± 0.02	$0.22^{+0.02}_{-0.01}$
VAPEC1 Norm.	$7.2^{+0.1}_{-1.3}\times10^{-4}$	$5.0^{+0.1}_{-0.3}\times10^{-4}$	$5.0^{+0.1}_{-0.3}\times10^{-4}$	$4.3^{+0.1}_{-0.3}\times10^{-4}$
VAPEC2 $k_{\rm B}T$ (keV)	$0.74^{+0.09}_{-0.03}$	0.62 ± 0.01	0.62 ± 0.01	$0.56^{+0.01}_{-0.03}$
VAPEC2 Norm.	$3.7^{+0.3}_{-0.8}\times10^{-4}$	$5.1\pm0.3\times10^{-4}$	$5.2^{+0.2}_{-0.3}\times10^{-4}$	$4.8\pm0.4\times10^{-4}$
Γ_3	$1.16^{+0.13}_{-0.10}$	$1.28^{+0.08}_{-0.12}$	$1.41^{+0.14}_{-0.09}$	$1.31^{+0.08}_{-0.10}$
PL3 Norm.[1]	$6.9^{+0.5}_{-0.3}\times10^{-4}$	$7.4^{+0.4}_{-0.5}\times10^{-4}$	$7.8^{+0.5}_{-0.9}\times10^{-4}$	$7.0^{+0.6}_{-0.3}\times10^{-4}$
$N_{\rm H,3}$ (/10^{22} cm^2)	0(fixed)	<0.03	<0.05	<0.03

Note. — Best-fit parameters for selected broadband models. All models include two absorbed X-ray power-laws (PL1, PL2), two VAPEC components, a third soft X-ray power-law (PL3), and Fe Kα and Kβ emission lines. Listed are: Model 5, where PL3 is not absorbed; Model 6, where PL3 is absorbed; Model 7, where ZVPHABS abundances are thawed for S, Ca, and Fe and fluorescent lines for Si, S, Ar, Ca and Ni are added; and Model 8, our best-fit model, in which the VAPEC abundances $Z_{\rm Ne} = 2.7\pm0.3$ and $Z_{\rm Mg} = 1.9\pm0.4$.
[1]: units are ph keV^{-1} cm^{-2} s^{-1} at 1 keV.

Table 3
Fluorescent Emission Line Parameters

Line	Energy Centroid (keV)	Intensity (10^{-5} ph cm^{-2} s^{-1})	$EW_{\rm obs}$ (eV)	$\Delta\chi^2$	F-test Prob.	$EW_{\rm calc}$ (eV)
Si Kα	1.71 ± 0.01	0.9 ± 0.2	24 ± 6	39.8	7.6×10^{-10}	26.3
S Kα	2.307 ± 0.016	0.8 ± 0.4	6 ± 2	5.0	9.6×10^{-2}	11.4
Ar Kα	2.994 ± 0.023	1.2 ± 0.5	13 ± 4	20.1	8.0×10^{-5}	4.7
Ca Kα	3.690 ± 0.023	1.8 ± 0.7	8 ± 3	6.2	5.4×10^{-2}	3.7
Fe Kα	6.394 ± 0.003	23.2 ± 1.0	83 ± 3	3077	$<1\times10^{-40}$	128
Fe Kβ	7.056^1	3.0^2	11^2	28.3	2.7×10^{-7}	17^2
Ni Kα	7.47 ± 0.05	1.4 ± 0.8	15 ± 5	9.3	1.1×10^{-2}	7.1

Note. — Results are for Model 8. Observed equivalent widths (Col. [4]) are determined relative to a locally-fit continuum. All widths were tied to that for the Fe Kα line, 14^{+10}_{-14} eV. $EW_{\rm calc}$ (Col. [7]) denotes predicted equivalent width values using Eq. 1 (uniform covering assuming line of sight column density), solar abundances, and a covering fraction of 1.0.
[1] denotes a fixed parameter.
[2] denotes value tied to 0.13 that for the Fe Kα line.

TABLE 4
HARD X-RAY ABSORPTION EDGES

K-shell Edge	ZVPHABS Abundance	Edge Energy (keV)	Edge Optical Depth, τ
S	$1.14^{+0.11}_{-0.15}$	$2.468^{+0.014}_{-0.011}$	$0.24^{+0.03}_{-0.06}$
Ca	$1.5^{+0.8}_{-0.6}$	4.040 ± 0.045	0.03 ± 0.01
Fe	$1.17^{+0.12}_{-0.09}$	7.103 ± 0.015	0.21 ± 0.01

Note. — The ZVPHABS abundances in Col. (2) are from Model 8. The edge energy and optical depths (cols. [3]-[4]) are from a model with ZVPHABS abundances for Fe, Ca and S set to zero and edges fit instead.

TABLE 5
ABUNDANCE RATIOS

Method	Ratio	Value
1	$Z_{\mathrm{O}}/Z_{\mathrm{Fe}}$	0.8 ± 0.4
1	$Z_{\mathrm{Ne}}/Z_{\mathrm{Fe}}$	2.3 ± 0.3
1	$Z_{\mathrm{Mg}}/Z_{\mathrm{Fe}}$	1.6 ± 0.3
3	$Z_{\mathrm{Si}}/Z_{\mathrm{Fe}}$	1.5 ± 0.4
2	$Z_{\mathrm{S}}/Z_{\mathrm{Fe}}$	1.0 ± 0.1
3	$Z_{\mathrm{S}}/Z_{\mathrm{Fe}}$	0.8 ± 0.3
3	$Z_{\mathrm{Ar}}/Z_{\mathrm{Fe}}$	4 ± 1
2	$Z_{\mathrm{Ca}}/Z_{\mathrm{Fe}}$	1.3 ± 0.6
3	$Z_{\mathrm{Ca}}/Z_{\mathrm{Fe}}$	3 ± 1
3	$Z_{\mathrm{Ni}}/Z_{\mathrm{Fe}}$	3 ± 1

Note. — Methods 1, 2, and 3 (Col. [1]) denote abundances derived from thermal plasma emission lines, K shell edge depths, and Kα fluorescent emission line intensities, respectively.
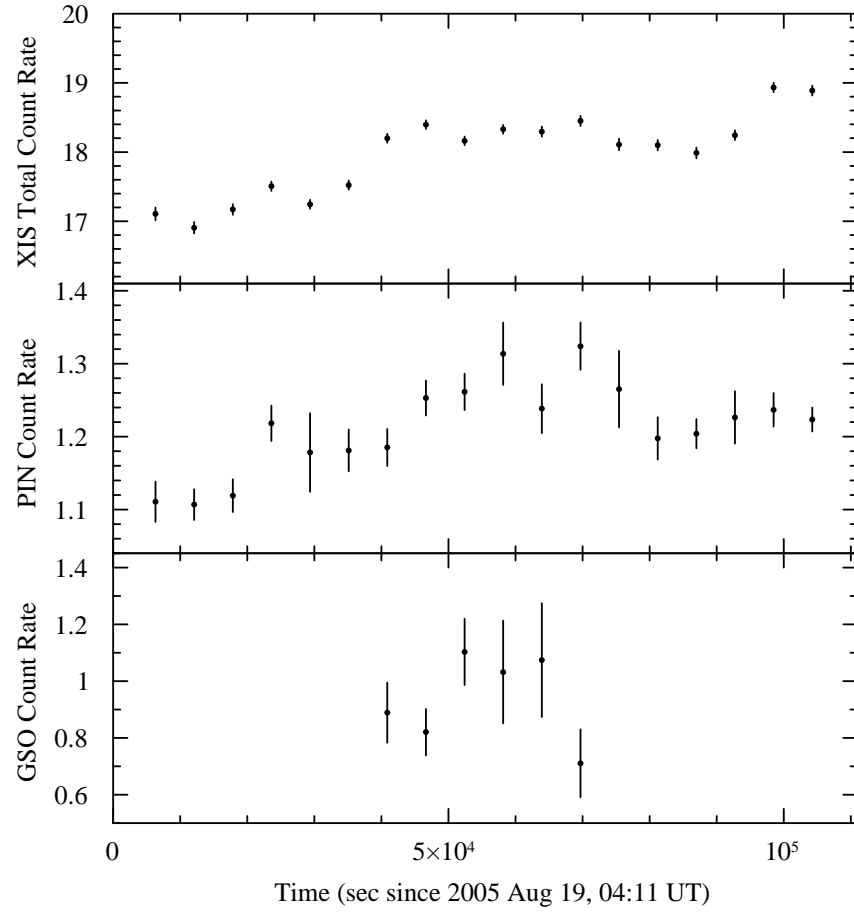
FIG. 1.— Orbitally binned XIS and HXD light curves. The top panel shows the 2–10 keV count rate light curve, summed over all four XIS cameras. The 12–76 keV HXD-PIN light curve is shown in the middle panel. The 45–250 keV HXD-GSO light curve is shown in the bottom panel.
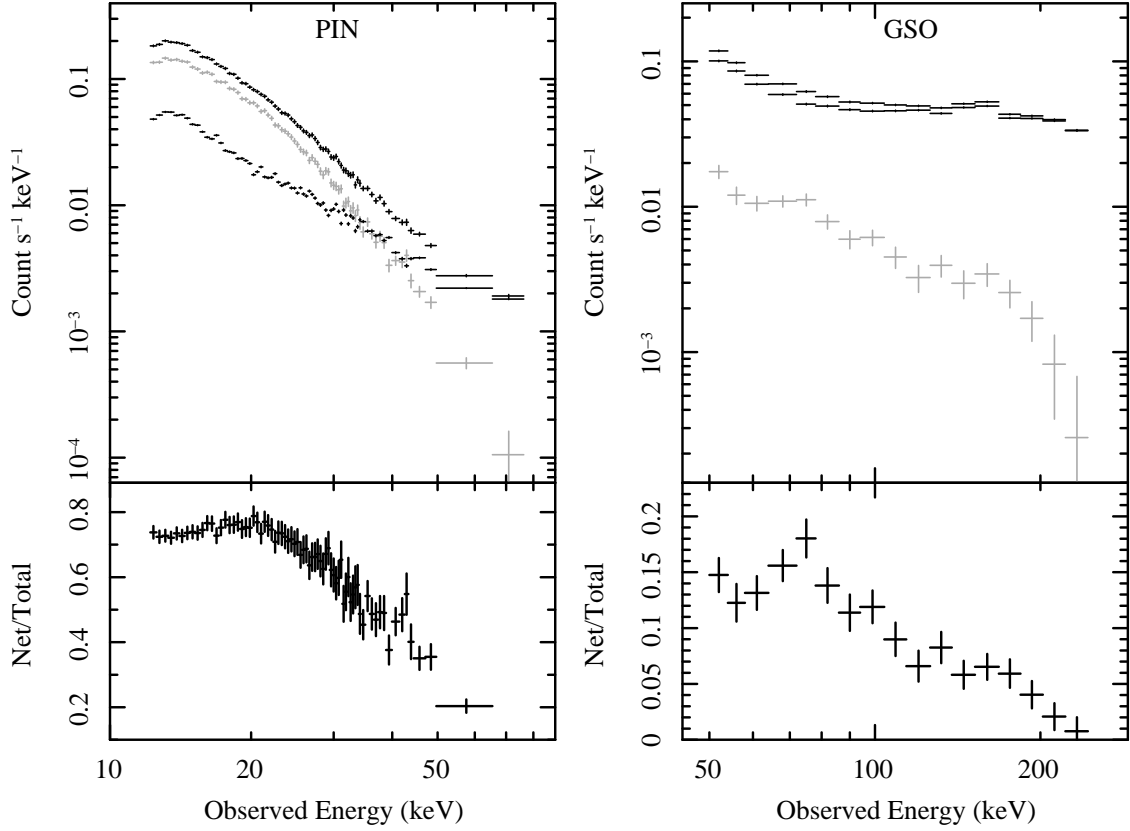
FIG. 2.— HXD-PIN (*left*) and GSO (*right*) spectra. The upper panels show the net source spectrum (*gray points*), the background (*lower black points*), and the total (source + background) spectrum (*upper black points*). The PIN spectra have been binned such that the net spectrum has a minimum signal-to-noise ratio of 10σ per bin. The GSO spectra have been binned as described in §2. The lower panels shows the ratio of the net source spectrum to the total spectrum.
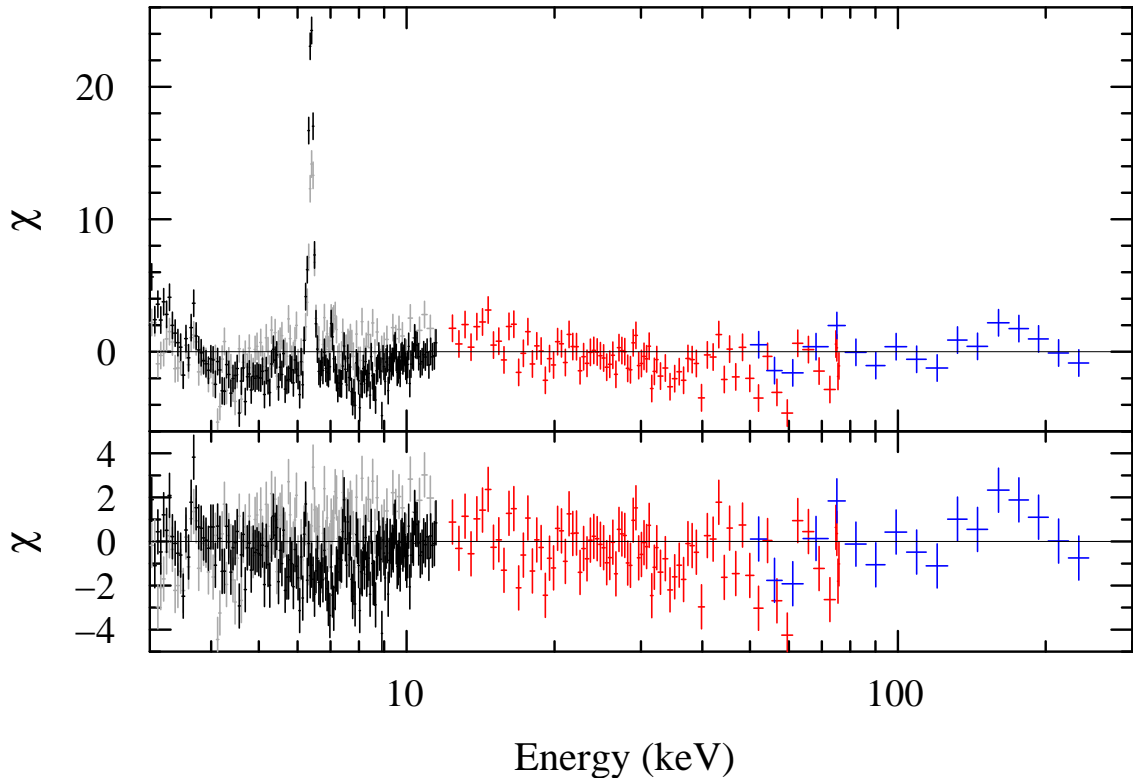
FIG. 3.— Residuals to Model 1, the single absorbed power-law (*top*, and Model 2, which included dual absorbed power-law components and Fe Kα and Kβ line emission (*bottom*). Black points denote the three FI XIS spectra, which have been co-added here for clarity. Gray, red and blue points denote XIS1, PIN, and GSO, respectively. Rest-frame energies are shown. The XIS data have been plotted with a binning factor of 10.
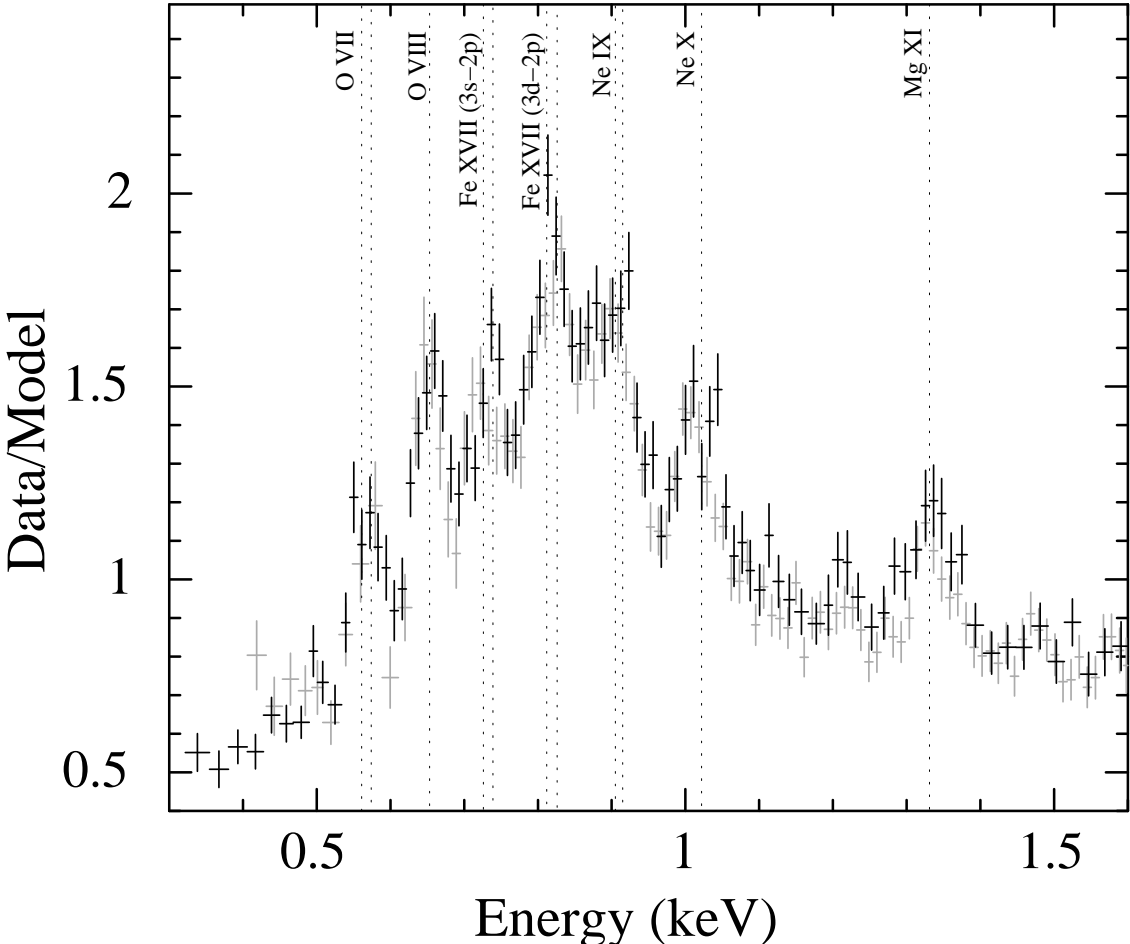
FIG. 4.— Ratio of the soft band data to a simple power-law, showing the prominent emission lines. Black points denote the XIS BI; gray points denote data from XIS0, 2 and 3, which have been co-added for clarity. Rest-frame energies are shown. The data have been plotted with a binning factor of 3.

Markowitz et al.
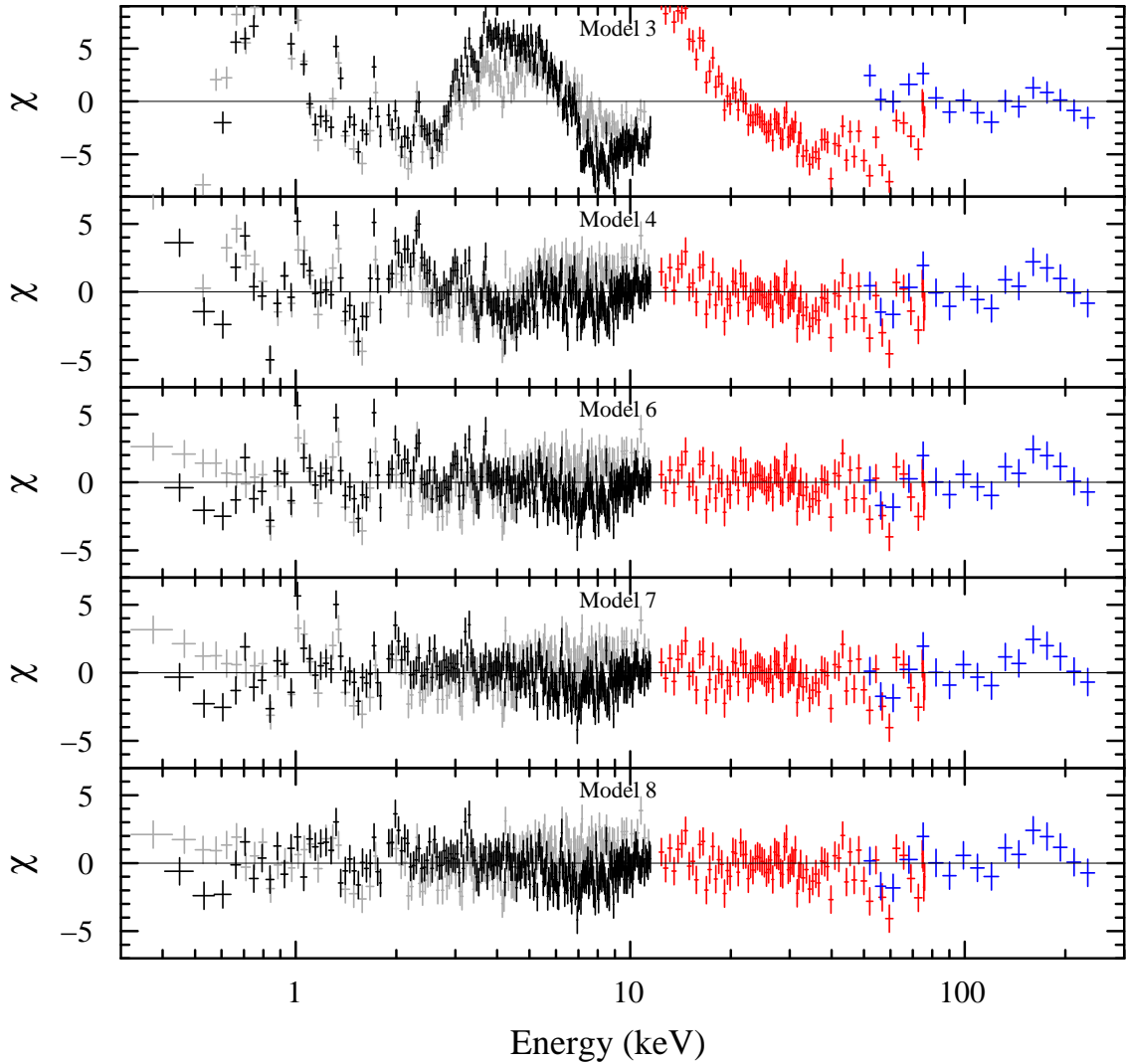
FIG. 5.— Residuals to various broadband models are shown. From top to bottom are: Model 3, with soft X-rays fit with a simple power-law; Model 4, with soft X-rays fit with two VAPEC components only; Model 6, with soft X-rays fit with two VAPEC components plus an absorbed power-law; Model 7, with K-shell absorption edges and Kα emission lines for S, Si, Ar, Ca and Ni fit; and Model 8, our best-fit model, with VAPEC abundances for Ne and Mg thawed. Black points denote the three FI XIS spectra, which have been co-added here for clarity. Gray, red and blue points denote XIS1, PIN, and GSO, respectively. Rest-frame energies are shown. The XIS data have been plotted with a binning factor of 10.
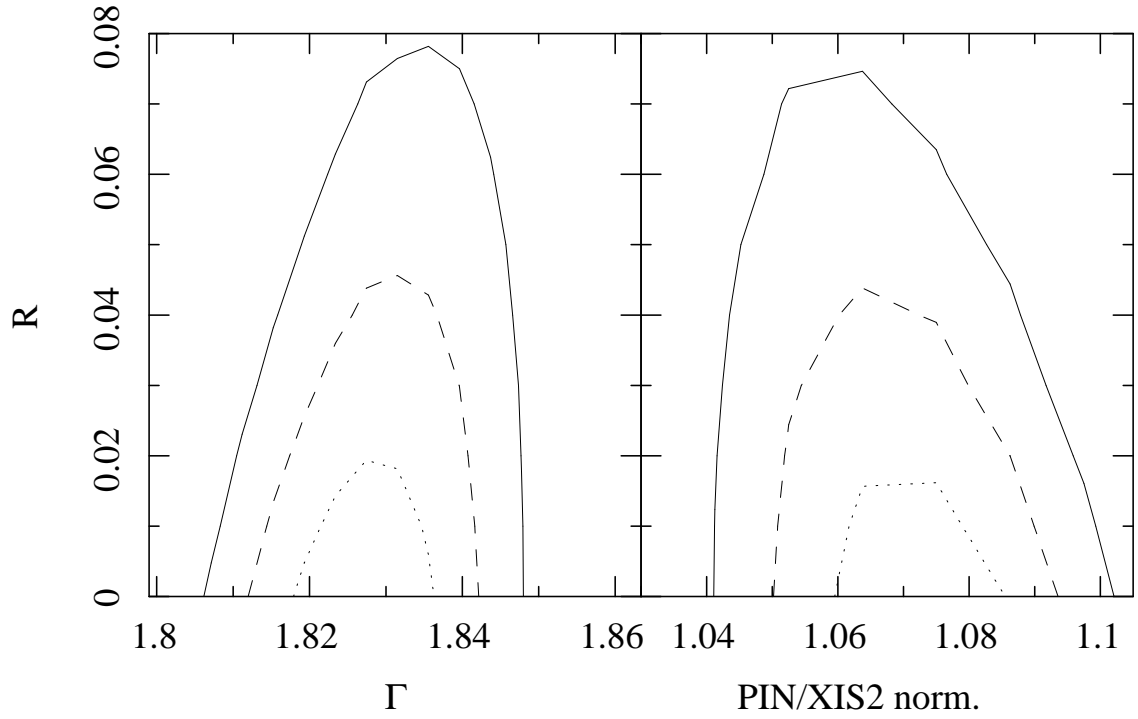
FIG. 6.— Contour plots of the Compton reflection fraction R versus the hard X-ray photon index $\Gamma_1 = \Gamma_2$ and the PIN/XIS2 instrument normalization for Model 8. Dotted, dashed, and solid lines denote 68, 95.4, and 99.73% confidence levels, respectively.
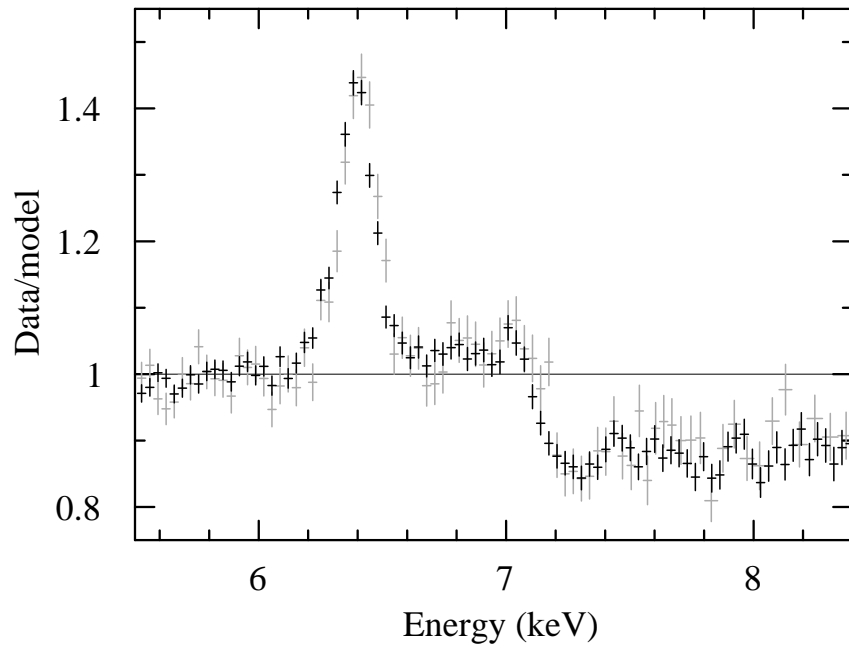
FIG. 7.— Residuals to a simple power-law model in the Fe K bandpass, showing the prominent Fe Kα emission line as well as the Fe Kβ line at 7.08±0.03 keV, the Ni Kα line at 7.47±0.05 keV, and the Fe K edge. Black points denote the three FI XIS spectra, which have been co-added for clarity; gray points denote XIS1. Rest-frame energies are shown. All data have been plotted with a binning factor of 10.
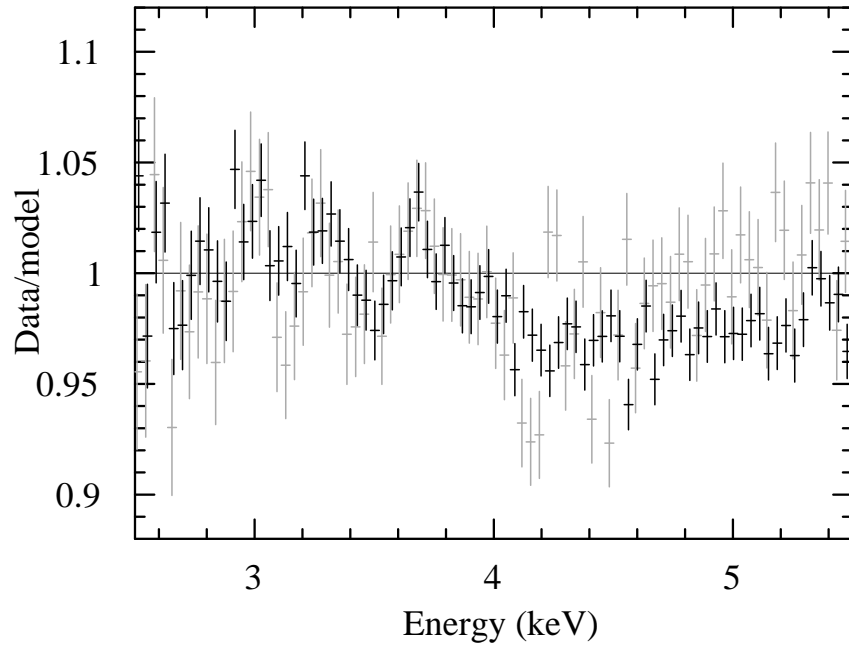
Markowitz et al.
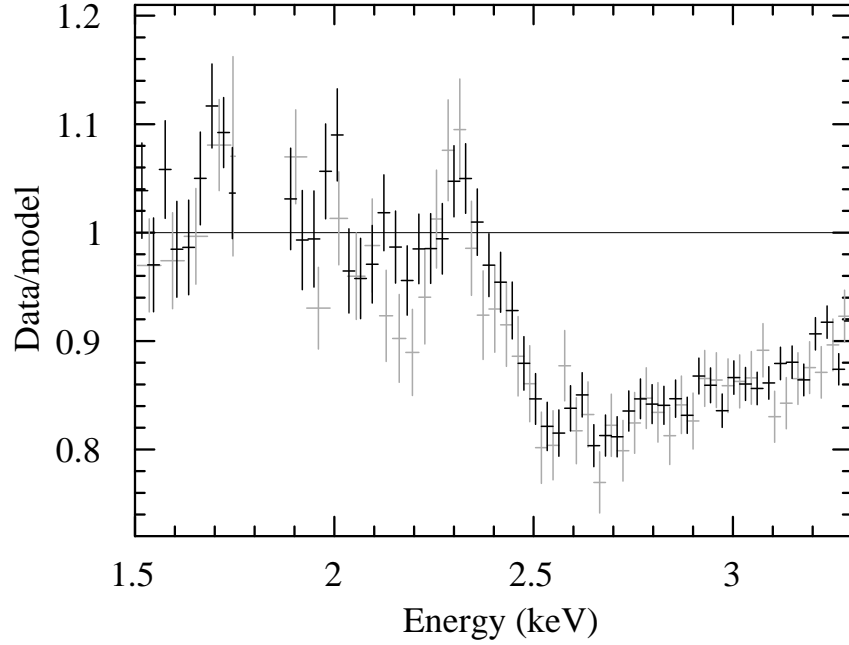
FIG. 8.— Residuals to a simple power-law model in the S K and Si K bandpass, showing the Si Kα emission line at 1.71±0.01 keV, the S Kα line at 2.307±0.016 keV, and the S K edge. Black points denote the three FI XIS spectra, which have been co-added for clarity; gray points denote XIS1. Rest-frame energies are shown. All data have been plotted with a binning factor of 10.

FIG. 9.— Residuals to a simple power-law model in the Ar K and Ca K bandpass, showing the Ar Kα emission line at 2.994±0.023 keV, the Ca Kα line at 3.690±0.023 keV, and the Ca K edge. Black points denote the three FI XIS spectra, which have been co-added for clarity; gray points denote XIS1. Rest-frame energies are shown. All data have been plotted with a binning factor of 10.
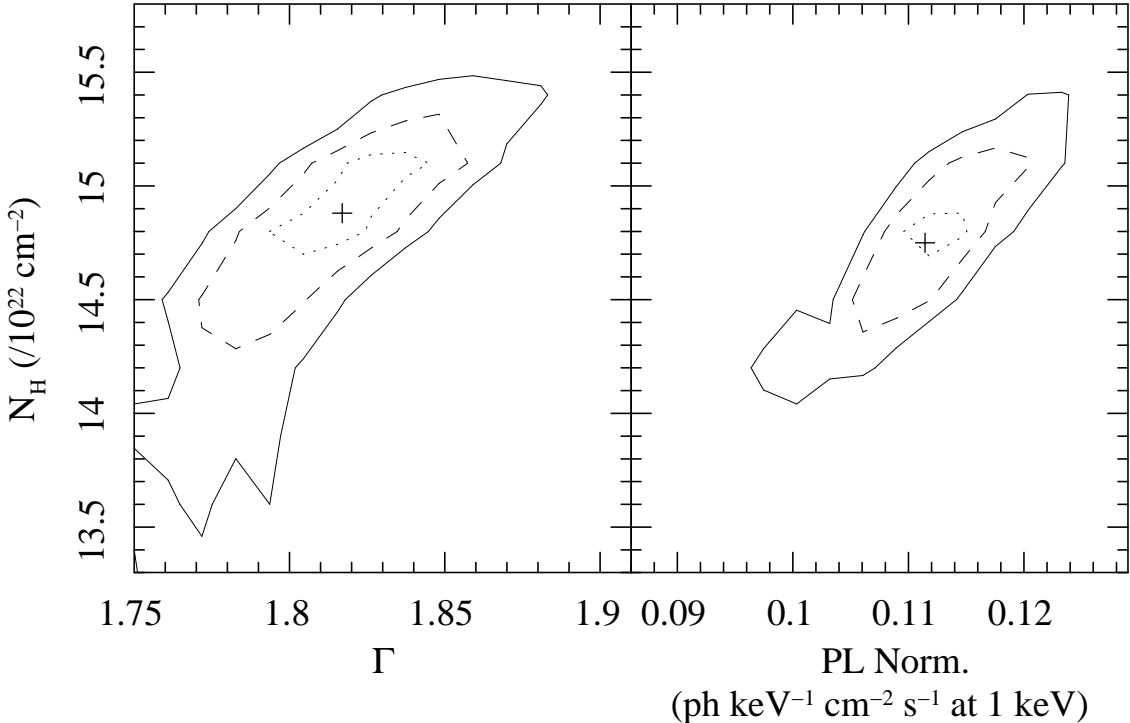
FIG. 10.— Contour plots of the line of sight column density absorbing the primary power-law versus the photon index (*left*) and 1 keV normalization (*right*) of the primary power-law component in Model 8. Dotted, dashed, and solid lines denote 68, 95.4, and 99.73% confidence levels, respectively. The plus signs mark the best-fit values.
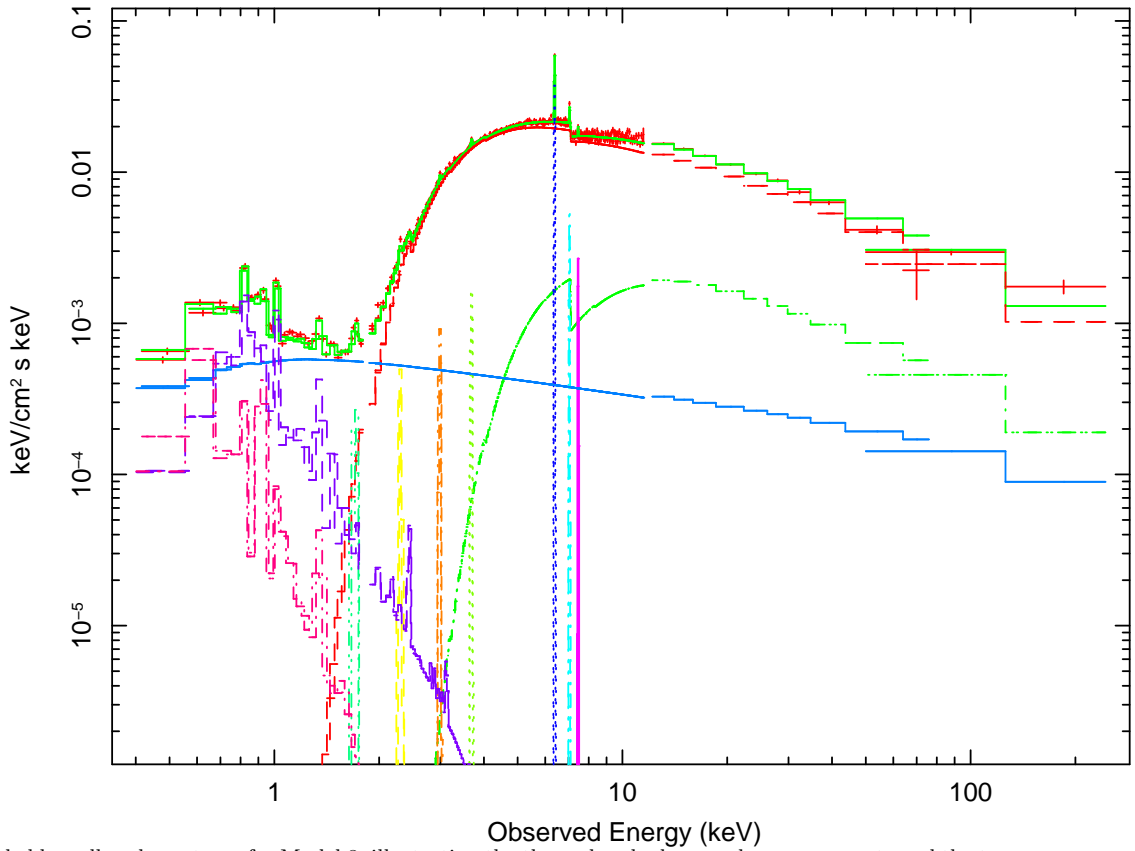
FIG. 11.— Unfolded broadband spectrum for Model 8, illustrating the three absorbed power-law components and the two VAPEC components. All data have been plotted with a binning factor of 10.
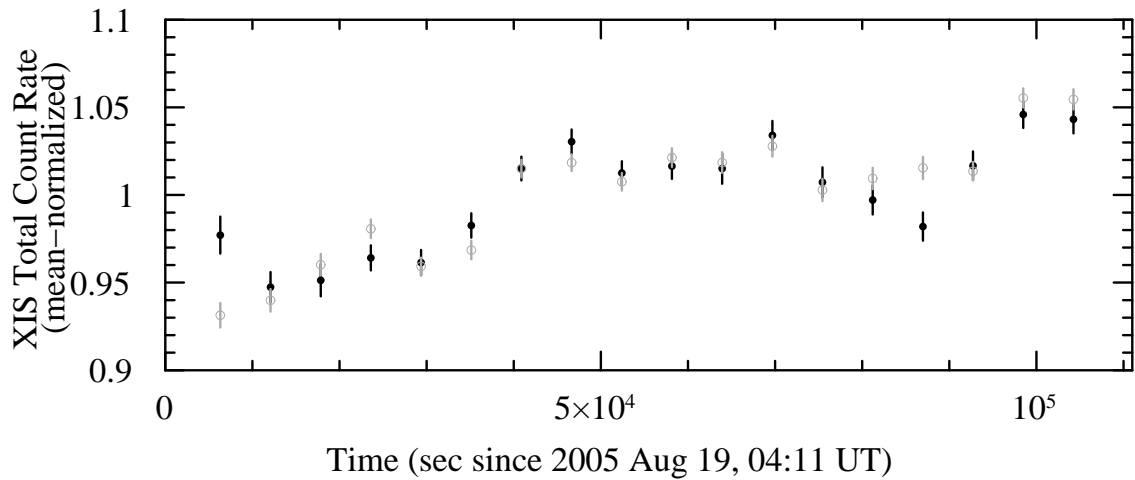

FIG. 12.— Mean-normalized, orbitally-binned 2–4 keV (*black filled circles*) and 5–10 keV (*gray open circles*) light curves, summed over all four XISes. Both light curves display very similar variability trends.